Acta Biomaterialia 135 (2021) 671–688

Contents lists available at ScienceDirect

Acta Biomaterialia

journal homepage: www.elsevier.com/locate/actbio

Full length article

Hydrothermal processing of 3D-printed calcium phosphate scaffolds enhances bone formation *in vivo*: a comparison with biomimetic treatment

Yago Raymond[a,b,c,d], Mar Bonany[a,b,c], Cyril Lehmann[a,b], Emilie Thorel[d], Raúl Benítez[c,e], Jordi Franch[f], Montserrat Espanol[a,b,c], Xavi Solé-Martí[a,b,c], Maria-Cristina Manzanares[g], Cristina Canal[a,b,c], Maria-Pau Ginebra[a,b,c,h,*]

[a] *Biomaterials, Biomechanics and Tissue Engineering Group, Department of Materials Science and Engineering, Universitat Politècnica de Catalunya (UPC), EEBE, Av. Eduard Maristany, 16, 08019 Barcelona, Spain*
[b] *Barcelona Research Centre for Multiscale Science and Engineering, UPC, EEBE, Av. Eduard Maristany, 10-14, 08019 Barcelona, Spain*
[c] *Biomedical Engineering Research Center (CREB), UPC, Av. Diagonal, 647, 08028 Barcelona, Spain*
[d] *Mimetis Biomaterials S.L., Carrer de Cartagena, 245, 3E, 08025 Barcelona, Spain*
[e] *Institut de Recerca Sant Joan de Déu (IRSJD), 39-57, 08950 Esplugues del Llobregat (Barcelona), Spain*
[f] *Bone Healing Group, Small Animal Surgery Department, Veterinary School, Universitat Autònoma de Barcelona, 08193 Bellaterra (Barcelona), Spain*
[g] *Human Anatomy and Embryology Unit, Department of Pathology and Experimental Therapeutics, Universitat de Barcelona, 08907 L'Hospitalet de Llobregat (Barcelona), Spain*
[h] *Institute for Bioengineering of Catalonia (IBEC), Barcelona Institute of Science and Technology, Carrer Baldiri Reixac 10- 12, 08028 Barcelona, Spain*

ARTICLE INFO

Article history:
Received 4 May 2021
Revised 2 August 2021
Accepted 1 September 2021
Available online 5 September 2021

Keywords:
3D printing
Bone scaffolds
Calcium phosphate
Biomimetic
Hydrothermal
In vivo

ABSTRACT

Hydrothermal (H) processes accelerate the hydrolysis reaction of α-tricalcium phosphate (α-TCP) compared to the long-established biomimetic (B) treatments. They are of special interest for patient-specific 3D-printed bone graft substitutes, where the manufacturing time represents a critical constraint. Altering the reaction conditions has implications for the physicochemical properties of the reaction product. However, the impact of the changes produced by the hydrothermal reaction on the *in vivo* performance was hitherto unknown. The present study compares the bone regeneration potential of 3D-printed α-TCP scaffolds hardened using these two treatments in rabbit condyle monocortical defects. Although both consolidation processes resulted in biocompatible scaffolds with osseointegrative and osteoconductive properties, the amount of newly formed bone increased by one third in the hydrothermal vs the biomimetic samples. B and H scaffolds consisted mostly of high specific surface area calcium-deficient hydroxyapatite (38 and 27 m^2 g^{-1}, respectively), with H samples containing also 10 wt.% β-tricalcium phosphate (β-TCP). The shrinkage produced during the consolidation process was shown to be very small in both cases, below 3%, and smaller for H than for B samples. The differences in the *in vivo* performance were mainly attributed to the distinct crystallisation nanostructures, which proved to have a major impact on permeability and protein adsorption capacity, using BSA as a model protein, with B samples being highly impermeable. Given the crucial role that soluble proteins play in osteogenesis, this is proposed to be a relevant factor behind the distinct *in vivo* performances observed for the two materials.

Statement of significance

The possibility to accelerate the consolidation of self-setting calcium phosphate inks through hydrothermal treatments has aroused great interest due to the associated advantages for the development of 3D-printed personalised bone scaffolds. Understanding the implications of this approach on the *in vivo* performance of the scaffolds is of paramount importance. This study compares, for the first time, this treat-

* Corresponding author at: Department of Materials Science and Engineering, Universitat Politècnica de Catalunya (UPC), EEBE, Av. Eduard Maristany, 16, 08019 Barcelona, Spain.
E-mail address: maria.pau.ginebra@upc.edu (M.-P. Ginebra).

https://doi.org/10.1016/j.actbio.2021.09.001
1742-7061/© 2021 The Author(s). Published by Elsevier Ltd on behalf of Acta Materialia Inc. This is an open access article under the CC BY-NC-ND license (http://creativecommons.org/licenses/by-nc-nd/4.0/)

ment to the long-established biomimetic setting strategy in terms of osteogenic potential *in vivo* in a rabbit model, and relates the results obtained to the physicochemical properties of the 3D-printed scaffolds (composition, crystallinity, nanostructure, nanoporosity) and their interaction with soluble proteins.
© 2021 The Author(s). Published by Elsevier Ltd on behalf of Acta Materialia Inc.
This is an open access article under the CC BY-NC-ND license
(http://creativecommons.org/licenses/by-nc-nd/4.0/)

1. Introduction

In recent years, the democratisation of additive manufacturing technologies has opened a wide variety of applications in the medical field [1]. Among them, patient-specific bone grafts and implants are one of the most straightforward and promising uses. These are already a reality in the medical industry. Personalised bone grafts are ideal for complex indications, *e.g.,* defects that are non-confined, geometrically complex, large, or that require vertical regeneration. The traditional solutions to these cases are autologous bone harvesting (usually fibula [2] and iliac crest [3]) or standard xenogeneic or synthetic blocks [4]. The main advantages of personalised bone scaffolds are: (1) Possibility of implementing a virtual surgical planning and more precisely tackle complex geometrical reconstructions [5–8]. (2) Shortening of the surgical time compared with the current available solutions [9,10]. (3) Reduction of the patient's morbidity by avoiding any additional surgery [11,12].

Among the wide variety of existing printing techniques, filamentary-based direct ink writing (DIW) stands as one of the most convenient for the fabrication of ceramic parts. This technology, consisting of the layer by layer microextrusion of a pasty ink [13], enables introducing high ceramic loads in the printed parts, presents low to non-existent waste of raw material, which is critical when using priced biomaterials, and is simple and affordable. It has been widely used with calcium phosphates [8,14–16], the most used materials for bone regeneration, due to their similarity to the natural bone and high biocompatibility [17]. Typically, calcium phosphate-based inks require a sintering process after printing the green body to achieve hardening of the printed structure.

Recently, self-setting calcium phosphate inks were developed, based on the hydrolysis of alpha tricalcium phosphate (α-TCP) [18,19]. In this case, the printed structures do not require a high-temperature sintering process, since the hardening is due to a cementitious reaction that takes place in the printed paste at room temperature. This avoids the densification process and the high volumetric changes in the printed structures occurring in the sintering process. A further advantage is that the reaction product of the hydrolysis of α-TCP is a calcium–deficient hydroxyapatite (CDHA) [20], with a composition closer to the bone mineral than that of the sintered calcium phosphates [21,22]. These biomimetic CDHA DIW scaffolds have been proved to exhibit adequate osteogenic properties [23–28]. However, the slowness of the hydrolysis reaction requires long times for the hardening of the 3D-printed structures, from 3 to 10 days depending on the powder reactivity and the nature of the ink binder used [18,19,27,29,30]. This limits the implementation of this technique in clinical applications, where bone grafts have to be designed and manufactured on-demand, usually in a reduced time span.

In this respect, it has been shown that it is possible to accelerate the hydrolysis reaction of α-TCP by hydrothermal routes [31,32]. This is a promising approach to reduce the lead time of DIW personalised bone grafts [33]. Nonetheless, besides accelerating the hydrolysis process, the hydrothermal process introduces modifications both in the chemistry and the microstructure of the final product, which can have implications in the final performance of the printed scaffolds. For instance, it has been reported that hydrothermal processes result in needle-shaped crystal nucleation instead of the plate-like structures obtained by biomimetic processing. This, in turn, leads to a wider nano-pore size distribution [33]. Moreover, the appearance of an additional crystalline phase (β-tricalcium phosphate, β-TCP) is recorded when using hydrothermal hardening strategies. Although recent studies have shown the key role of surface texture and crystal morphology in the osteogenic properties of calcium phosphates [34–37], the impact that this specific hydrothermal treatment may have on the bone regeneration potential is unknown.

With this in mind, the aim of this work is to shed light on the effect of the biomimetic and hydrothermal processing on the morphological and physicochemical features of 3D-printed calcium phosphate scaffolds and to analyse the effect of the resulting composition and textural parameters on the *in vivo* performance of the 3D-printed scaffolds in an orthotopic rabbit model.

2. Materials and methods

2.1. Scaffold preparation

An ink consisting of a ceramic suspension was obtained by mixing a 30 wt.% poloxamer 407 aqueous solution with α-TCP powder (Innotere, Germany) at a liquid to powder ratio of 0.45 wt./wt. The poloxamer solution formed a gel that guaranteed the stable dispersion of the ceramic particles and conferred the adequate pseudoplastic rheological properties to the ink, as characterised in a previous study [38]. The resulting paste was extruded immediately after mixing with a custom-made DIW 3D printer. The scaffolds were printed with a nozzle with an orifice diameter of 413 µm (22 ga. tapered tip, Fisnar, WI, USA) following an orthogonal pattern, with a strand-to-strand separation of 250 µm and a layer height of 307 µm. Two scaffold geometries were printed: cubic samples with 8 mm side and cylindrical samples with 8 mm in diameter and height. The samples were hardened using two different processes, either i) a biomimetic treatment consisting of a 7-day immersion in water at 37 °C; or ii) a hydrothermal treatment, using temperature to accelerate the process, specifically autoclaving at 121 °C, as described in a previous work [33]. After the hardening process, the cylindrical samples were water-sanded in their lateral face with P1200-grain sandpaper down to a final diameter of 5 mm for the *in vivo* experiments. The particles originated during the sanding process were removed by three rinsing and sonication steps in distilled water. The hydrothermally set scaffolds were sterilised by wet heat in an autoclave, while the biomimetic samples were sterilised by gamma irradiation (25 KGy dose) to avoid heating them above the physiological temperature.

2.2. Characterisation of the scaffolds

2.2.1. Chemical characterisation

The phase composition of the scaffolds was assessed by X-ray diffraction (XRD) using a diffractometer (D8 Advance Eco, Bruker AXS GmbH, Germany) equipped with a Cu K-α beam, a Ni filter and a LynxEye detector. Measurements were acquired in the 3-65° 2θ range with a step size of 0.02° and a sampling step time of

3 sec. The quantification of the crystalline phases and the determination of amorphous content were performed by Rietveld refinement (TOPAS 5, Bruker, MA, USA). The amount of amorphous phase was indirectly determined by the addition of corundum as internal standard (a known amount between 30 and 40 wt.%). The amorphous content (A) was deduced from the overestimation of the quantity of internal standard following Eq. (1) [39]:

$$A = \frac{100\%}{100\% - R} \cdot 100\% \cdot \left(1 - \frac{R}{R_R}\right) \quad (1)$$

Where R corresponds to the added amount of internal standard and R_R corresponds to the percentage of corundum calculated in the Rietveld refinement. In the refinement process, the following crystal structures were employed: calcium-deficient hydroxyapatite (COD-9002214), β-tricalcium phosphate (ICSD-006191) and corundum (ICSD-033639), obtained either from the inorganic crystal structure database (ICSD) or the crystallography open database (COD). The following parameters were adjusted in the refinement: lattice parameters, phase scale factors, zero-shift error, peak shape parameters and preferred orientation (Appendix A).

In addition, the crystallite size (D_i) and the deviation associated with the uncertainty ($\sigma^2(D_i)$) of the value were determined following Eq. (2) and Eq. (3), respectively [40].

$$D_i = \frac{180}{\pi} \cdot \frac{\lambda}{(W - W_{st})^{0.5}} \quad (2)$$

$$\sigma^2(D_i) = \frac{\left(\frac{180\lambda}{\pi}\right)^2}{4(W - W_{st})^3}\left[\sigma^2(W) + \sigma^2(W_{st})\right] \quad (3)$$

Where λ corresponds to the wavelength of the X- rays, W to the Caglioti coefficient associated to the diffractogram of the sample and W_{st} to that of a standard sample measured in the same conditions (LaB_6). The Caglioti term in Eq. (2) [41] was refined for the whole diffractogram.

Raman spectra of the powdered scaffolds were recorded using an inVia™ Qontor® spectrometer (Renishaw, UK). A 532 nm laser with a 10 mW output power was used as the excitation source. All the spectra were collected with a 50x objective, in the 400–4000 cm^{-1} range, using an integration time of 10 sec and 5 accumulations. The spectral resolution was ca. 1 cm^{-1}.

The amount of poloxamer 407 remaining in the final scaffolds was determined for both experimental conditions. The total organic carbon content (TOC) was assessed with an organic elemental analyser (FLASH 2000 CHNS/O, Thermo Scientific, MA, USA) performing a combustion at 1200 °C in an oxygen atmosphere.

2.2.2. Microstructure, porosity and pore architecture

Different techniques were used to assess the morphology of the scaffolds at different magnifications. The microstructure of the samples was observed through scanning electron microscopy (FIB/SEM, Neon 40, Zeiss, Germany) run at 5 kV and acquired with a through-the-lens electron detector. Prior to the acquisition, samples were sputter-coated with a thin electron-conductive carbon layer to prevent electrostatic charges (Emitech 950x carbon evaporator, France). The specific surface area (SSA) was determined by nitrogen sorption using the Brunauer-Emmett-Teller (BET) method (ASAP 2020, Micromeritics, GA, USA). Before the analysis, the samples were degassed by holding them at 100 °C for 2 h under a 10 mmHg vaccum atmosphere. The skeletal density (ρ_{skel}) of the specimens was determined by helium pycnometry (AccuPyc 1330, Micromeritics, GA, USA). The apparent density (ρ_{app}) of the scaffolds was calculated as the quotient of the dry scaffold's mass over its equivalent volume measured on the cubic samples (n = 15), and the total porosity was determined as $[1-(\rho_{app}/\rho_{skel})]\bullet 100$. The pore entrance size distribution in the range of 0.006 to 360 µm was determined by mercury intrusion porosimetry (MIP). The MIP results were combined with the skeletal density to determine the internal porosity of the strands (intrastrand porosity), according to Eq. (4):

$$P_{intrastrand} = \left(\frac{V_{(p<10\mu m)}}{V_{(p<10\mu m)} + V_{mat}}\right) \cdot 100 = \left(\frac{V_{(p<10\mu m)}}{V_{(p<10\mu m)} + {}^{1}/_{\rho_{skel}}}\right) \cdot 100 \quad (4)$$

Where $V_{(p<10\mu m)}$ is the volume of pores smaller than 10 µm normalised per unit of mass, obtained from the sum of the incremental mercury intrusion in the pores below this size in the pore entrance size distribution curves, and V_{mat} is the specific volume of the material, which is the reciprocal of the skeletal density.

The morphology of the scaffold's architecture was assessed by micro-computed tomography (µ-CT) (Skyscan 1272, Bruker, MA, USA) operated with an X-ray current of 111 µA and an acceleration voltage of 90 kV. The X-ray beam was configured with an aluminium and a copper filter with respective thicknesses of 0.5 and 0.038 mm. The exposure time and step resolution around the 180° were set to 1650 ms and 0.2° per step, respectively. No frame averaging was applied. The acquisition was performed with an isotropic voxel resolution of 18 µm. The data were processed with beam hardening correction and object shifting correction, and reconstructed into tomographic image stacks (NRecon software, Bruker, MA, USA). Subsequently, the resulting reconstructions were aligned to the printing axis (DataViewer software, Bruker, MA, USA). Different strategies were followed to evaluate the morphological differences between the printed structures and the theoretical geometry. First, the different orthogonal views of the structure were assessed with an image analysis software (ImageJ2, NIH, MD, USA [42]) to calculate the percentage of linear shrinkage in the three printer axis directions (*i.e.,* X, Y and Z). For each direction, the distance corresponding to five repetition units was measured and compared with the theoretical dimensions calculating the percentual deviation. Five samples per condition were analysed. Subsequently, the macroporosity generated during the printing process was measured (CTAn v1.16 software, Bruker, MA, USA) and compared to that of the theoretical structure, generated through CAD software (SolidWorks, Dassault Systèmes, France) based on the dimensions introduced in the printing configuration, transformed to image stack (Mimics, Materialise, Belgium), and analysed with the same procedure used for the µ-CT experimental acquisitions. Finally, the two different structures were compared with the theoretical mesh design: A 3D mesh of a representative sample was obtained for each condition by segmenting the µ-CT acquisition (Slicer v4.10.2, 3D Slicer, NIH, USA [43]) and a design of the theoretical structure was created with CAD software (MeshMixer v3.5, Autodesk, CA, USA). Then, a 3D point cloud comparison software (CloudCompare v2.11.2, EDF R&D, France) was used to assess the deviation of the printed structures with respect to the reference theoretical design. Briefly, a point cloud was sampled from the mesh of the printed and the normal distance from each point of the 3D cloud to the reference mesh was calculated. A colour map of the deviation distances on the 3D structure was obtained. Moreover, the sample deviation distance of each point of the 3D cloud was recorded for both conditions and compared in a histogram.

2.2.3. Mechanical characterisation

A uniaxial compression test was performed to determine the ultimate compressive strength and compression modulus of the scaffolds. For this purpose, 8 mm cubic scaffolds were compressed (Bionix servo-hydraulic test system, MTS Systems, MN, USA) in the Z printing direction in displacement-control mode at a displacement rate of 1 mm min^{-1}. For each condition, 15 samples were tested. Furthermore, a 3-point bending test was performed to determine the ultimate flexural strength, the flexural modulus

and the work of fracture of the samples. The flexural test was executed following the ISO 14704:2016 standard [44]. 3D-printed blocks 50 mm in length, 4 mm in width and 3 mm in height (coinciding with the printer X, Y and Z axis, respectively) were tested using a hybrid rheometer (Discovery HR-3, TA instruments, Germany) equipped with a 3-point bending clamp with a span of 40 mm. The test was run until fracture under displacement-control mode at a crosshead speed of 0.5 mm min^{-1}. A total of 21 samples were tested per condition. In both cases the samples were tested in wet conditions to better simulate the *in vivo* situation. Prior to the tests the scaffolds were immersed in distilled water and stored overnight at 37 °C. The Weibull modulus was calculated following the procedure described elsewhere [33].

2.2.4. Protein adsorption study

To analyse the relevance of microstructural features in the interaction with proteins in solution, a study was carried out with bovine serum albumin (BSA) as a model protein. BSA (Sigma Aldrich, MO, USA) was dissolved in phosphate-buffered saline (PBS, Gibco, TX, USA) at two different concentrations, 600 µg ml^{-1} and 6000 µg ml^{-1}. BSA was fluorescently marked with 3-(4-carboxybenxoyl)quinoline-2-carboxaldehyde (CBQCA, Invitrogen, MA, USA) following the manufacturer's indications. In order to visualise the protein penetration in the strands' cross-section, 5 mm-length spare strands of each material were immersed in 150 µl of each BSA solution, for different incubation times (*i.e.,* 30 min, 1 h, 2 h, 4 h, 8 h and 24 h). The adsorbed protein was imaged by means of a fluorescence confocal microscope (LSM 800, Zeiss, Germany) using a wavelength of 488 nm. A flat surface of the strand cross-section was obtained by embedding the samples in two-part epoxy resin (Sei Whale, R*Concept, Spain) and water sanding them down to P4000 grain size (EcoMet 4 grinder polisher, Buehler, IL, USA). Additionally, an indirect quantification of the kinetics of protein adsorption was performed. For each of the studied time points, 5 mg of B and H strands were incubated in 100 µl of both BSA solutions. The supernatants were collected and their fluorescence intensity measured in a microplate reader (Synergy HTX, BioTek Instruments, VT, USA). Data were correlated to a calibration curve to establish the BSA concentration remaining in the supernatants. These concentrations were subtracted from the initial known solutions' concentration to determine the amount of protein adsorbed by the strands. The results were normalised by the sample weight and SSA of each material.

2.3. In vitro study

2.3.1. Cell culture

Osteoblast-like MG-63 cells (ATCC, VA, USA) were cultured in DMEM (Gibco, CA, USA) supplemented with 10% foetal bovine serum (FBS), 2 mM L-glutamine, penicillin/streptomycin (50 U ml^{-1} and 50 µg ml^{-1}, respectively) and 20 mM 4-(2-hydroxyethyl)-1-piperazineethanesulfonic acid (HEPES), all from Gibco. HEPES was used as a pH buffer to prevent the acidification of the medium by CDHA [45,46]. Cells were expanded and maintained at 37 °C, 95% humidity and 5% CO_2.

Before cell seeding, scaffolds of both experimental conditions were preconditioned for 48 h in 2 ml of complete DMEM. Afterwards, the medium was removed and the cells were seeded on top of the scaffolds (4×10^5 cells in 50 µl DMEM / scaffold) and incubated for 1 h to allow cell attachment. Subsequently, 2 ml of fresh medium were gently added. The samples were incubated for 6 h, 3 days, 7 days and 14 days, renewing the medium every other day.

2.3.2. Cell adhesion and proliferation

Cells were rinsed with PBS at each time point and fixed with 4% paraformaldehyde solution (PFA, Sigma-Aldrich, MO, USA). Afterwards, cells were immersed for 15 min in 0.05% Triton X-100 solution in PBS. Actin filaments were stained with Alexa Fluor 546-conjugated phalloidin (Invitrogen, CA, USA, 1:400 in PBS) and nuclei were stained with 4',6-diamidino-2-phenylindole (DAPI, LifeTechnologies, CA, USA, 1 µg ml^{-1} in PBS). Images were captured by means of a confocal laser scanning microscope (LSM 800, Zeiss, Germany). Cell adhesion was further evaluated by observing the samples after 6 h of culture with SEM (JSM-7001F, JEOL, Japan). The samples were prepared by fixing the cells with 4% PFA solution, dehydrating them in an increasing series of ethanol solutions and sputtering with carbon (EMITECH K950X Turbo Evaporator, Quorum Technologies Ltd., UK). Moreover, cell proliferation was determined using a resazurin-based viability reagent (PrestoBlue, Invitrogen, MA, USA) following the manufacturer's instructions.

2.3.3. Cell differentiation

Alkaline phosphatase (ALP) activity was measured using an ALP assay kit (SensoLyte pNPP, Anaspec, CA, USA). At each time point, the scaffolds were placed in a new well plate and rinsed with PBS. Subsequently, the cells were lysed with 500 µl of mammalian protein extraction reagent (M-PER, ThermoFisher, MA, USA) and incubated with p-nitrophenyl phosphate (pNPP) solution at 37 °C for 60 min. Absorbance measurements were performed using a microplate reader (Synergy HTX, BioTek Instruments, VT, USA) at 405 nm wavelength. Data were normalised to cell number at each condition. To do so, lactate dehydrogenase (LDH) detection kit (Roche, Germany) was used to quantify the release of LDH from the M-PER lysates following the manufacturer's indications. Finally, absorbance was measured in the microplate reader at 492 nm wavelength.

2.3.4. Ion exchange

The ionic interaction of the scaffolds with the cell culture medium was assessed by quantifying the Ca^{2+} and P_i fluctuations in the supernatants collected at each change of medium. The measurements were performed by inductively coupled plasma - optical emission spectroscopy (ICP-OES, 5100 SVDV, Agilent Technologies, Japan). Prior to the analysis, the supernatants were diluted 1:10 in a solution of 2% HNO_3 (69% HNO_3 TMA Hyperpur, PanReac AppliChem, Germany). 44Ca and 31P signals were calibrated against a multi-element standard solution (Inorganic Ventures, VA, USA).

2.4. In vivo study

2.4.1. Study design

All animal procedures were performed in compliance with the Guide for Care and Use of Laboratory Animals [47] and the European Community Guidelines (Directive 2010/63/EU) for the protection of animals used for scientific purposes and under the permission of the National Animal Ethics Committee on Human and Animal Experimentation (Approval # CEAAH 4683). This study was part of a larger study to analyse the bone regeneration capacity of scaffolds with different configurations. In total ten adult female New Zealand White (NZW) rabbits with a bodyweight ranging from 4.8–5.5 kg and an age range of 8–12 months were used. The animals were purchased from a professional stock breeder (Charles River Laboratories, France) and housed in individual boxes of two square meters each one and an acclimatisation period of two weeks was established prior to surgery. Health status was determined by physical and orthopaedic examination, radiographic examination of the rear limbs and results of hematologic and serum biochemical profiles.

Cylindrical 3D-printed scaffolds with 5 mm in diameter and 8 mm in height, fabricated by either the biomimetic or the hydrothermal protocols (n = 7 for each condition) were randomly

inserted in bilateral defects drilled in the medial aspect of the femoral condyle. One single time point at 8 weeks was evaluated.

2.4.2. Surgical procedure

The surgical procedure was performed under standard sterile conditions. The animals were pre-anaesthetised using butorphanol, midazolam and medetomidine. Anaesthesia was induced with propofol and maintained with inhaled isoflurane in an oxygen carrier by mask. Both limbs stifle areas were clipped and subsequently scrubbed with chlorhexidine gluconate solution for an aseptic preparation of the surgical field. With the animals in dorsal recumbency and after a small skin subcutaneous and joint capsule incision, the medial aspect of both femoral condyles was exposed by a medial parapatellar incision (Fig. 1ii). Using a 2.5 mm drill bit and under copious physiological saline irrigation to avoid thermal necrosis, a monocortical bone defect was performed in the centre point of the medial aspect of the condyle (Fig. 1iii). Afterwards, the defect was enlarged with a 5 mm drill always under continuous physiological saline irrigation (Fig. 1iv). The depth of the defect was fixed to 10 mm. The cylindrical scaffolds with a diameter of 5 mm and a height of 10 mm were then press-fitted in each bone defect (Fig. 1v, vi). After assuring the stability of the implants, the joint capsule, the subcutaneous tissue and the skin were sutured in layers in a routine way (Fig. 1vii, viii).

Once recovered from the anaesthesia, the animals were housed in the same individual boxes and allowed to full weight-bearing. During the postoperative period, analgesic and antibiotic treatments were given to the animals for 7 days.

The animals were euthanised 8 weeks after the surgical procedure with an overdose of sodium pentobarbital according to the legislation of the American Veterinary Medical Association (AVMA). A pre-euthanasia sedation of midazolam and medetomidine was used for animal welfare reasons.

After euthanasia, the condylar regions of the femur were explanted and fixed in 10% neutral-buffered formalin solution for two weeks and dehydrated in an increasing series of ethanol solutions.

2.4.3. Histomorphometric analysis

This process was based on X-ray micro-computed tomography (µ-CT) of the explants and allowed to quantify in threedimensions the amount and distribution of the newly formed bone into the scaffold. The analysis was composed of the following steps:

- *Acquisition:* The dehydrated samples were analysed by µ-CT, adjusting the settings described in Section 2.2.2 to a higher resolution, to properly distinguish the different tissue regions. The exposure time per projection was 2600 ms, 1800 projections were done along the 360° and an averaging of 3 frames per projection was chosen. An isotropic voxel size of 10 µm was used. The acquisitions were reconstructed using the same procedure previously described.
- *Segmentation:* The reconstructed stacks were first oriented in the Z printing direction and the X and Y printing axis were aligned to the image axis (Data Viewer, Bruker, MA, USA). Then, a cylindrical volume of interest (VOI) corresponding to the scaffold region (Fig. 2i) was defined (CTAn, Bruker, MA, USA). The images of each z-stack were processed individually by fitting a univariate Gaussian mixture model with four components to their pixel grayscale level distributions [48]. This approach modelled the grayscale image histograms as a weighted sum of four Gaussian distributions corresponding to biomaterial, bone, non-mineralised tissue and outer VOI (Fig. 2ii). The model allowed clustering each pixel into one of the four tissue-type groups according to its greyscale value (Fig. 2iii). This process was run iteratively for each image of the stack along the Z-direction. Subsequently, the segmented images were processed with a median filter with a disc-shaped structuring element of radius 50 µm to remove the segmentation artefacts attributed to the noise in the image (Fig. 2iv).
- *Quantification of the Bone Volume Percentage*: For each sample, the total number of segmented pixels classified under the different tissue-type labels were quantified. Then, the bone volume percentage was calculated as the total number of bone pixels over the total number of available volume pixels.
- *Quantification of the Radial Bone Intrusion Curves:* The bone fraction in the scaffolds was measured and plotted as a function of the radial distance from the surface. To do so, the samples were analysed in radial bands using a thinning algorithm based on a morphological erosion transformation [49]. For each image of the Z stack, the perimeter of the VOI was taken as a departure point to determine a 100 µm-thick band by using a disc erosion operation. Then the percentage of bone in available volume was calculated for this band. This process was repeated successively departing from the new perimeter obtained after subtracting the previous band moving through the centre of the scaffold with each iteration.
- *Representation of the Bone Distribution Axial Colormaps:* For each condition, all the segmented stacks were added into a single 3-dimensional matrix stacking them along the Z printing axis (*i.e.*, the axial direction of the cylindrical VOI). Then, the bone fraction of the resulting matrix was calculated for the Z projection. As a result, a 2D image representing in each pixel the average bone fraction of all the samples for the corresponding X-Y coordinate was obtained and plotted as a colour map.

The program developed to perform the image analysis was written in Python (Python 3.9.0, www.python.org), its main stages are detailed in Appendix B and the code is available in a Git repository (https://github.com/YAGORAYMOND/uCT-image-analysis).

2.4.4. Histological assessment

After µ-CT analysis, the dehydrated samples were immersed in solutions with increasing concentrations (*i.e.*, 25, 50, 75 and 100%) of methyl methacrylate resin (Technovit 7200 VLC, Germany). The embedded samples were stored overnight under vaccum and photopolymerised in a UV lamp (EXAKT 520, Exakt Technologies, Germany). The resulting blocks were cut through the central axis of the scaffolds cylinder with a precision diamond band saw (EXAKT 300 CP, Exakt Technologies, Germany).

The cut surface of the first half sample was water sanded down to P4000 grain size (Surface grinder, EXAKT 400 CS, AW110, Exakt Technologies, Germany), coated with a thin carbon layer and observed with a scanning electron microscope (SEM, Phenom XL, Phenom World, MA, USA) operated at 10 kV and using a backscattered electron detector. Mappings of the full samples were acquired with the SEM automatic image mapping scan utility (Automated image mapping software, Phenom ProSuite, Phenom World, MA, USA).

A 300 µm slice of the second half-sample was cut with a precision band saw with a diamond blade, glued to a PMMA 3 mm sample holder (precision adhesive press, EXAKT 402, Exakt Technologies, Germany), polished down to 30–50 µm and stained using Masson-Goldner trichrome staining. The stained samples were observed with a bright-field optical microscope (BX51-P, Olympus, Japan).

2.5. Statistical analysis

The compressive strength and the dimensional evaluation of the structures are reported as mean values ± standard deviations. The histomorphometric analysis is reported with a boxplot indicating the median and quartiles. A statistical analysis software

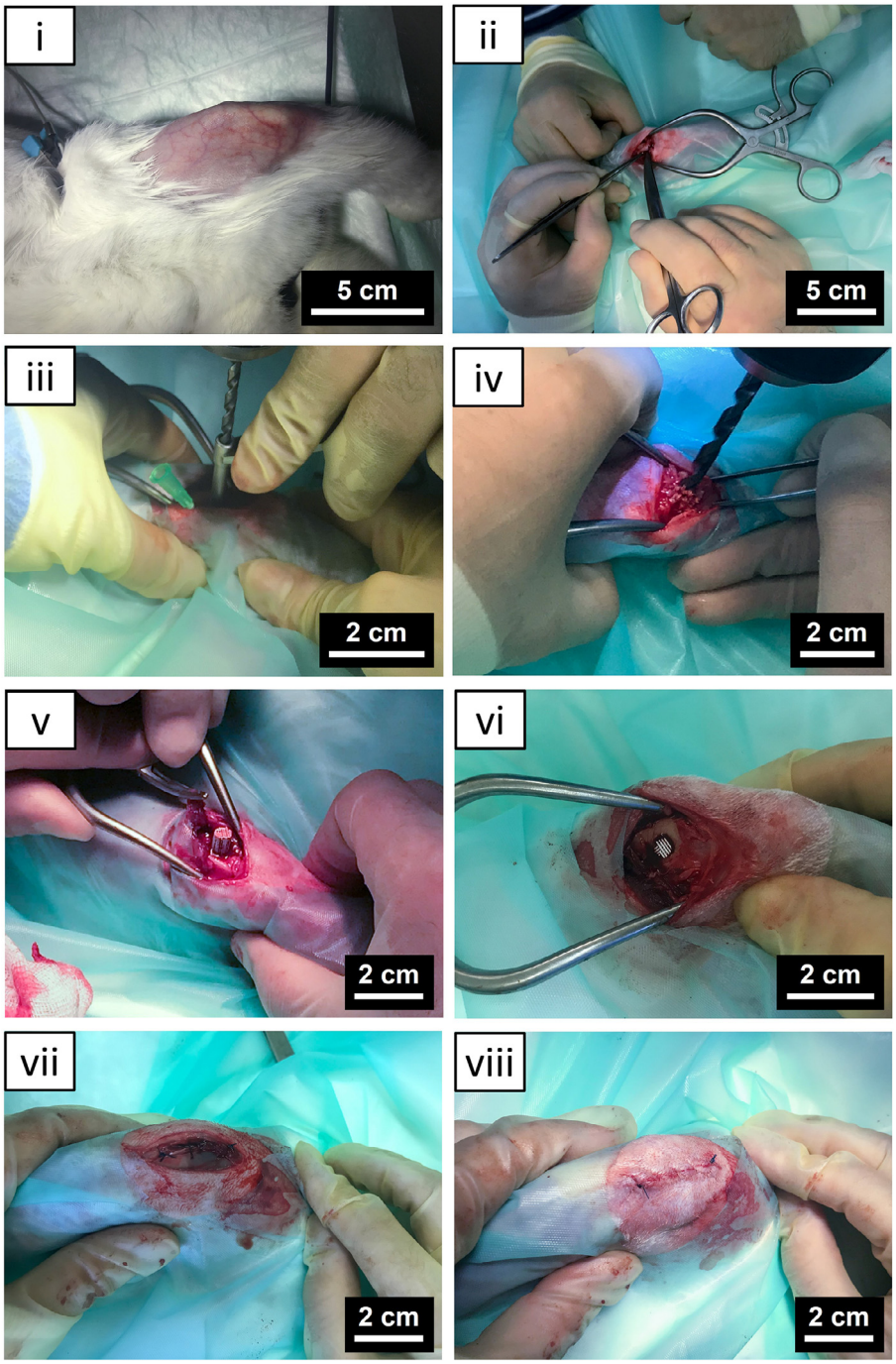

Fig. 1. (i) Defect region pre-operatory preparation. (ii) Medial parapatellar incision in the femoral condyle. (iii) 2.5 mm drilling in the centre point of the medial aspect of the femoral condyle guided by a drill guide. (iv) Expansion of the initial guide hole to 5 mm. (v, vi) Press-fit grafting of the cylindrical scaffold. (vii) Suture of the joint capsule. (viii) Suture of the skin.

(Minitab®19, MiniTab Inc., PA, USA) was used in all the cases to determine statistically significant differences between specimens by one-way analysis of variance (ANOVA) followed by Tukey's post hoc test. A confidence interval of 95% ($\alpha = 0.05$) was considered.

3. Results

3.1. Scaffolds characterisation

3.1.1. Chemical composition

Differences in chemical composition were observed by XRD of both biomaterials (Fig. 3i). Whilst all diffraction peaks in the biomimetic scaffold, apart from the corundum peaks corresponding to the internal standard, were attributed to CDHA, the hydrothermal scaffolds presented a biphasic composition consisting of CDHA and β-TCP. Additionally, differences in the sharpness of the peaks were readily visible for the hydrothermal condition when compared to the biomimetic one. Better resolved peaks indicating a higher degree of crystallinity were observed for the hydrothermally treated scaffolds (Fig. 3ii). This was translated into larger average crystallite size values for the hydrothermal as compared to the biomimetic scaffolds (54.4 ± 3.1 nm versus 27.5 ± 1.2 nm, respectively). In addition, in both XRD spectra, the peak appearing at 25.9° corresponding to the (002) reflection

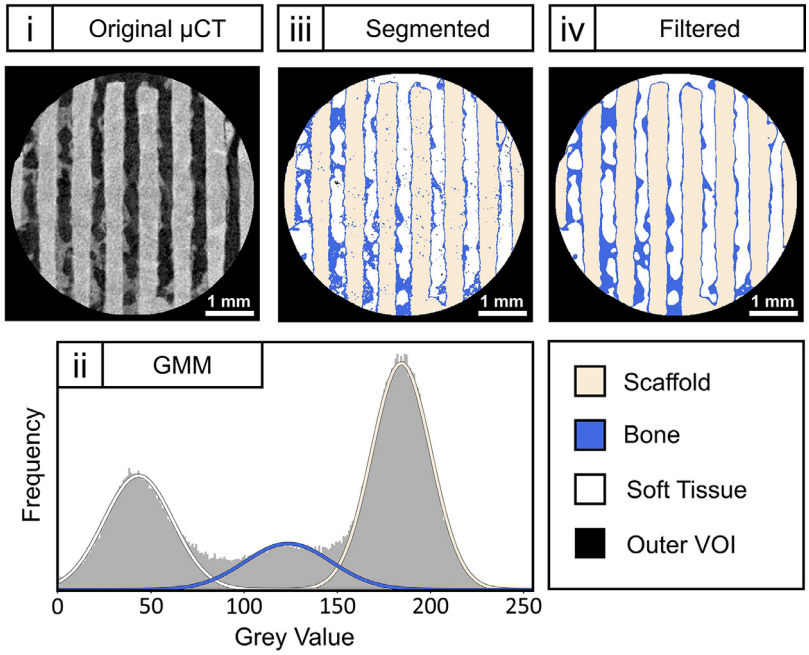

Fig. 2. Segmentation process: (i) slice image of the stack after orientation through Z printing axis and definition of a VOI, (ii) grey values histogram (background) with the Gaussian Mixture Model (GMM) distributions fitted for each tissue type, (iii) image after segmentation with the three model sub-populations and (iv) segmented image after applying median filter (disk-shaped structuring element with radius 50 µm) to correct for erroneously assigned pixels due to image noise. For visualisation purposes, pixels corresponding to outer VOI background have been excluded from the histogram representation.

of CDHA, was substantially sharper than the rest of the peaks of the same phase, indicating a preferential crystal growth along the *c* axis direction. Changes in the relative intensity of the peaks were also detected in the 31.0–33.5° 2θ range, which were attributed to both the peak overlapping of the additional phase encountered and the texturisation of the anisotropic crystals during the sample preparation. Moreover, although XRD provides direct information on crystalline phases, the addition of a known amount of an internal standard mixed with the powdered scaffolds allows also an indirect determination of the amount of amorphous phases present in the samples [39]. The resulting XRD spectra along with the results of phase quantification by Rietveld refinement, revealed that the biomimetic treatment resulted in 92.9% of CDHA and 7.1% of amorphous phase, compared to 78.7% of CDHA, 10.1% β-TCP and 11.2% of amorphous phase obtained with the hydrothermal treatment.

The analysis by Raman spectroscopy showed similar results for both treatments presenting the characteristic PO_4 vibration v_1 band at ≈ 960 cm^{-1}. Furthermore, two v_2 (PO_4) vibrations corresponding to the doubly degenerate bending mode O-P-O appearing at 447 and 433 cm^{-1}, the v_3 (PO_4) vibrations corresponding to the triply degenerate asymmetric stretching mode (P-O) appearing in the region from 1030 to 1100 cm^{-1} and the v_4 (PO_4) triply degenerate bending mode vibrations appearing in the region 550–630 cm^{-1} [50]. The weak band at ≈ 1005 cm^{-1} is assigned to the symmetric stretching of the HPO_4^{2-} ions, the band at ≈ 880 cm^{-1} to the stretching of P-(OH) in HPO_4^{2-} and the band at 3572 cm^{-1} is associated with the stretching mode of the OH^- group [51].

The final amount of poloxamer 407 in the scaffolds was determined by TOC. Organic carbon contents of 0.52 wt.% and 0.40 wt.% were found in the biomimetic and hydrothermally treated samples, respectively. Considering the molecular structure of poloxamer 407, this corresponds to 0.85 wt.% of poloxamer 407 remaining in the samples obtained by the biomimetic process and 0.65 wt.% in those obtained by the hydrothermal process.

3.1.2. Microstructure, porosity, mechanical properties and protein adsorption

The scaffolds presented remarkable differences in the microstructure. Whilst the samples set under biomimetic conditions presented a microstructure consisting of entangled plate-like hydroxyapatite nanocrystals, the samples hardened by hydrothermal routes showed interlocked acicular needle-shaped nanocrystals, with a much larger aspect ratio, as displayed in Fig. 4. The plate-like crystals of the biomimetic samples resulted in a larger SSA of 38.54 m^2 g^{-1} compared to 27.11 m^2 g^{-1} for the hydrothermal samples.

The total porosity of the scaffolds, determined by gravimetric methods, was similar in the two scaffold types, irrespective of the consolidation method (Table 1). The macroporosity (P_{macro}) calculated by µ-CT (Table 1) was slightly smaller for the hydrothermal than for the biomimetic samples. In both conditions, the values were slightly above the theoretical values. Regarding size distribution as determined by MIP, both samples presented a bimodal pore entrance size distribution (Fig. 5i), with two peaks corresponding to the intrastrand porosity, which was in the nanometric range and the interstrand porosity or macroporosity. Due to their large dimensions, the macropores fell partially outside the range detectable by this technique. Remarkable differences were found both in the intrastrand nanoporosity (Table 1) and nanopore size. Whereas the biomimetic samples presented a nanoporosity of 48.4% and nanopore sizes centred at 0.017 µm, the hydrothermally treated samples had a higher nanoporosity of 57.1%, with larger pore entrance sizes of 0.062 µm.

The assessment of the scaffolds' architecture by µ-CT revealed that both hardening treatments resulted in a small linear shrinkage. This shrinkage was mainly observed in the directions of the printing plane (*i.e.,* X and Y) with a more accentuated contraction of ≈ 3% for the biomimetic condition compared to ≈ 1.5% for the hydrothermal samples (Fig. 5ii), although the differences were not statistically significant. Accordingly, the mesh comparison of the 3D-printed structures (obtained by µ-CT) with the theoretical design (obtained through CAD) showed a global deviation through

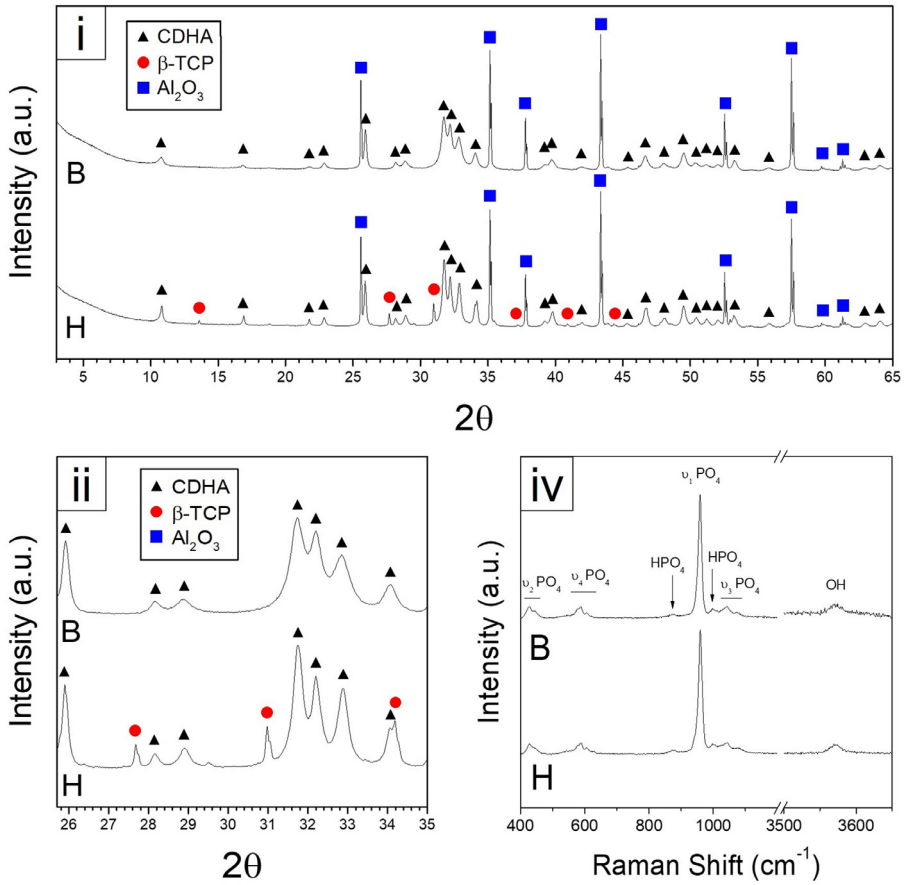

iii

	Crystalline Phase		Amorphous Phase	Crystallite Size
	CDHA	β-TCP		
Biomimetic	92.9 %	–	7.1 %	27.5 ± 1.2 nm
Hydrothermal	78.7 %	10.1 %	11.2 %	54.4 ± 3.1 nm

Fig. 3. Comparison of the samples set through the biomimetic (B) and hydrothermal (H) treatments: (i) X-ray diffraction pattern of the whole acquired 2θ range (3–65°) with symbols identifying the crystalline phases found in each sample, *i.e.*, calcium-deficient hydroxyapatite (CDHA), β-tricalcium phosphate (β-TCP) and corundum (Al_2O_3), the internal pattern added to the pristine samples to quantify the amorphous phase; (ii) zoomed region of the XRD diffractogram; (iii) Rietveld refinement quantification: crystalline and amorphous phase percentages and crystallite sizes; (iv) Raman spectra of the B and H samples.

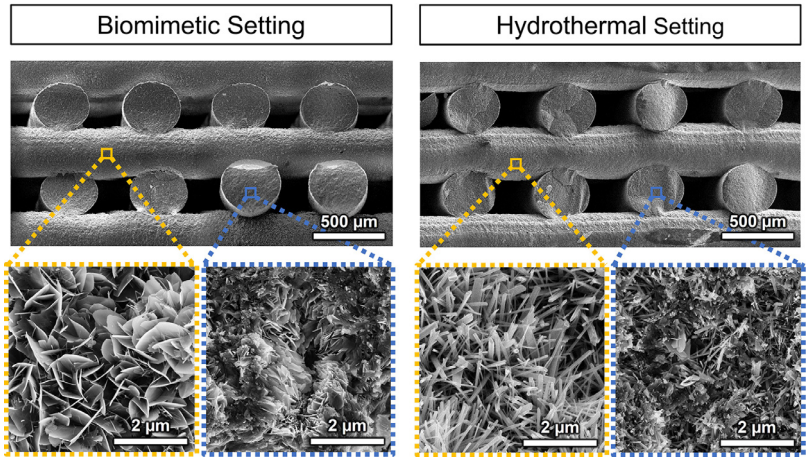

Fig. 4. Comparison of the macro- and microstructure of the scaffolds set under biomimetic and hydrothermal treatments assessed by scanning electron microscopy.

Table 1
Textural parameters of the scaffolds hardened using biomimetic or hydrothermal treatments: macroporosity (P_{macro}) obtained by µ-CT; intrastrand nanoporosity ($P_{intrastrand}$) measured combining MIP and He pycnometry according to Eq. (2); total porosity (P_{total}) determined by gravimetric methods; skeletal density (ρ_{skel}) determined by He pycnometry and specific surface area (SSA) by nitrogen adsorption through the BET method.

	P_{macro}* [%]	$P_{intrastrand}$ [%]	P_{total} [%]	ρ_{skel} [g.cm^{-3}]	SSA [mm^2.g^{-1}]
Biomimetic	44.47 ± 0.74	48.41	74.71 ± 2.02	3.01	38.54
Hydrothermal	41.08 ± 1.50	57.07	75.79 ± 1.07	3.06	27.11
p-value	0.002	-	0.091	-	-
Theoretical	39.58	-	-	-	-

Asterisks indicate statistically significant differences ($p < 0.05$). Values represented as: mean value ± standard deviation.

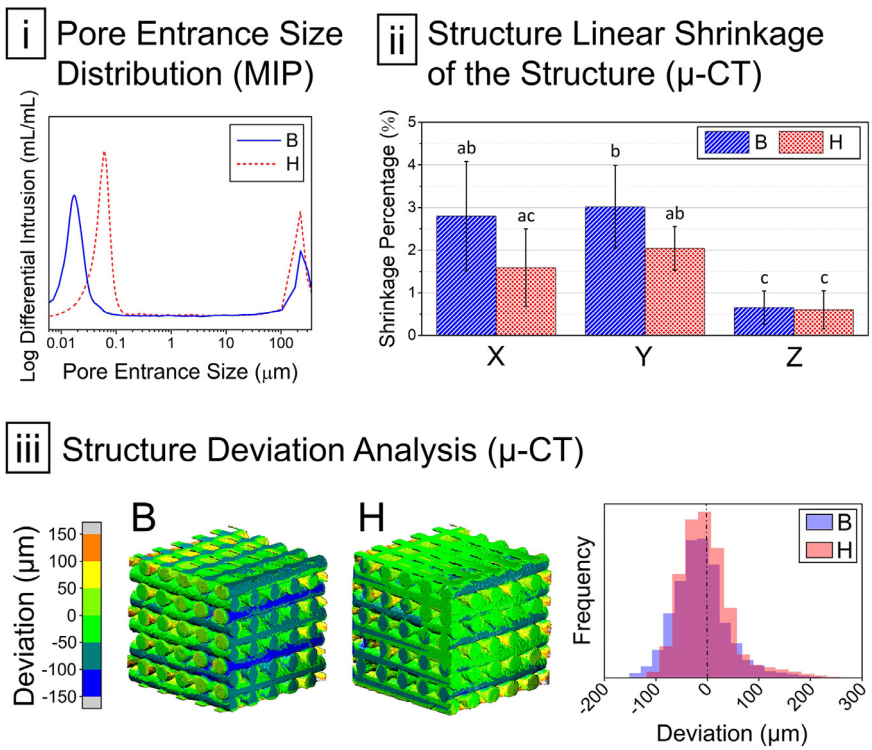

Fig. 5. Porosity analysis of the biomimetic and hydrothermally treated scaffolds (i) Pore entrance size distribution determined by mercury intrusion porosimetry (MIP). (ii) Linear shrinkage percentage calculated from µ-CT acquisitions (different letters indicating statistically significant differences, $p < 0.05$). (iii) 3D-mesh-based analysis of the scaffold morphology deviation compared to the theoretical structure. Meshes of each condition obtained by µ-CT segmentation. Colour map representing the local deviations in each region of the structure (top) and histogram representing the point-cloud deviation distribution (bottom).

Table 2
Mechanical properties of the 3D-printed scaffolds hardened with either biomimetic or hydrothermal treatments determined by uniaxial compression and 3-point bending tests.

	Compression		Flexion		
	Ultimate Compressive Strength* [MPa]	Compression Modulus* [MPa]	Ultimate Flexural Strength* [MPa]	Flexural Modulus [MPa]	Work of Fracture* [J.m^{-2}]
Biomimetic	3.33 ± 1.29 (2.73)	237 ± 84 (3.30)	0.65 ± 0.38 (1.90)	718 ± 348 (2.15)	2.05 ± 0.84 (2.42)
Hydrothermal	4.61 ± 1.38 (4.03)	366 ± 157 (2.94)	1.38 ± 0.24 (6.76)	730 ± 244 (3.44)	3.95 ± 0.81 (5.74)
p-value	0.014	0.009	0.000	0.887	0.000

Asterisks indicate statistically significant differences ($p < 0.05$). Values represented as: mean value ± standard deviation and Weibull modulus in parenthesis.

the negative values. This was noticeable in the colour map, with predominant lime-green colours, and in the histogram, with a shift through the left of both distributions (Fig. 5iii).

Regarding the mechanical properties (Table 2), the hydrothermal treatment provided approximately twice the strength achieved with the biomimetic treatment in either compression or flexion modes. On the other hand, the compression and flexural modulus were very similar in both treatments. Furthermore, higher Weibull modulus values were generally found for the hydrothermal condition, indicating that a higher reproducibility is achieved with this treatment.

3.1.3. Protein adsorption

Remarkable differences were found in the BSA adsorption patterns of the two materials. The penetration of the protein into the material was significantly higher in the H samples than in the B samples, as visualised in Fig. 6i. While in B samples the protein was detected only in a superficial layer of the strand, penetrating

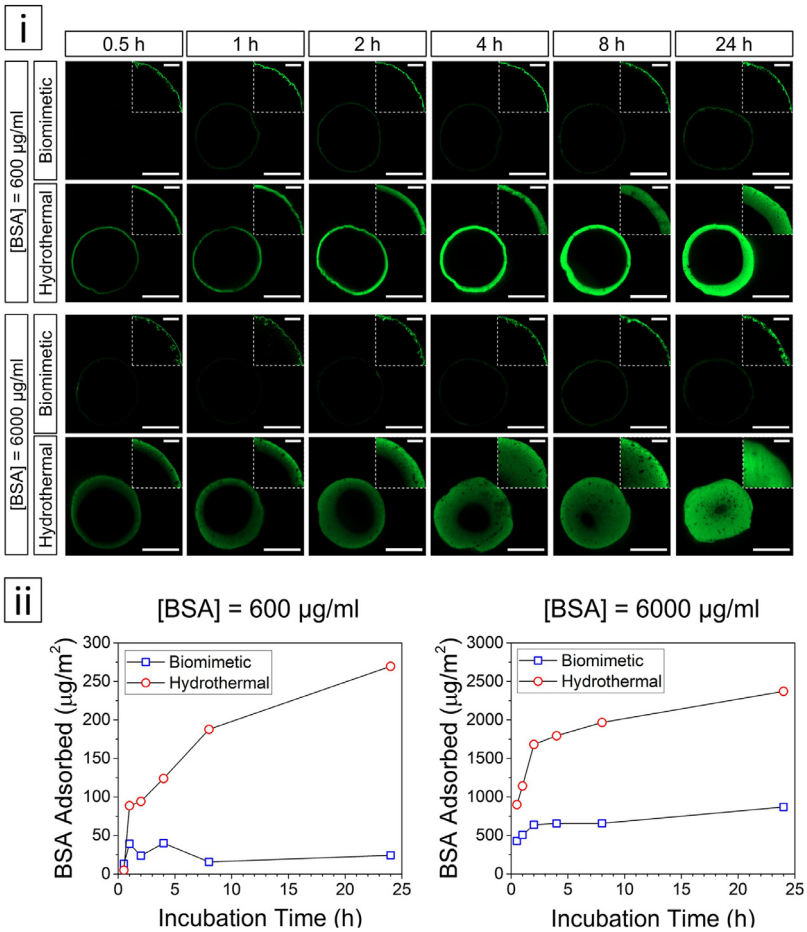

Fig. 6. Comparison of the protein adsorption properties of the biomimetic and hydrothermally treated samples incubated in two different BSA concentrations. (i) Fluorescent confocal microscopy images of the strand's cross-sections illustrating the penetration of BSA (in green) at different incubation times. Main images acquired with normalised settings for a better comparison between conditions. Scalebar = 200 µm. Inserts showing a close-up view of the surface penetration with optimised settings individually adjusted for each image. Scalebar = 50 µm. (ii) BSA adsorbed by the strands after incubation in the protein solutions. Results normalised by sample weight and SSA of each condition. (For interpretation of the references to color in this figure legend, the reader is referred to the web version of this article.)

only a few microns even after 24 h immersion, in H samples the protein diffused through the material progressively with incubation time. This was amplified in the solution with higher BSA concentration. These results were in agreement with the values of BSA adsorbed in each material calculated from the remaining protein in solution, as shown in Fig. 6ii for both H and B samples.

3.2. In vitro *study*

3.2.1. Cell performance

The *in vitro* study allowed to compare cell adhesion, proliferation and differentiation on the scaffolds hardened by the two different treatments. Fluorescence confocal microscopy (Fig. 7i) revealed that the cells were able to attach and proliferate in both scaffolds. The attached cells presented rounded morphologies initially, and progressively spread and proliferated until completely covering the surface of both scaffold types (Fig. 7i). A closer view (Fig. 7ii) shows that the cells at 6 h were able to start spreading and interacted with both microstructures, covering the CDHA nanocrystals regardless of their shape. Furthermore, cell viability quantification (Fig. 7iii) evidenced that the number of initially attached cells was approximately twice as high on the biomimetic scaffolds as on the hydrothermal counterparts, and similar exponential growth rates were observed in the two conditions. Finally, ALP activity (Fig. 7iv) was used to study the level of differentiation. A progressive increase in the ALP level was found, with no statistically significant differences between the two groups at each time point.

3.2.2. Ion exchange

The ionic interaction of both types of scaffolds with the cell culture medium was assessed during the course of the *in vitro* study. The trends followed by the two experimental conditions (B and H) were very similar. Despite the two days of preconditioning the samples absorbed Ca^{2+} and also, although to a lesser extent, P_i ions from the medium. The uptake was higher at the shorter time points and was progressively reduced, although the ionic concentration was below that of the culture medium throughout the whole study period.

3.3. In vivo *performance*

Surgeries were uneventful. However, one of the animals did not fully recover from the surgery, did not gain weight and finally died a few days after the procedure, which resulted in the loss of two samples, both belonging to group B. The rest of the animals completed a normal postoperative period without any clinical complication. No signs of infection, wound dehiscence, weight loss, behaviour changes, implant migration or lameness were observed along the postoperative period.

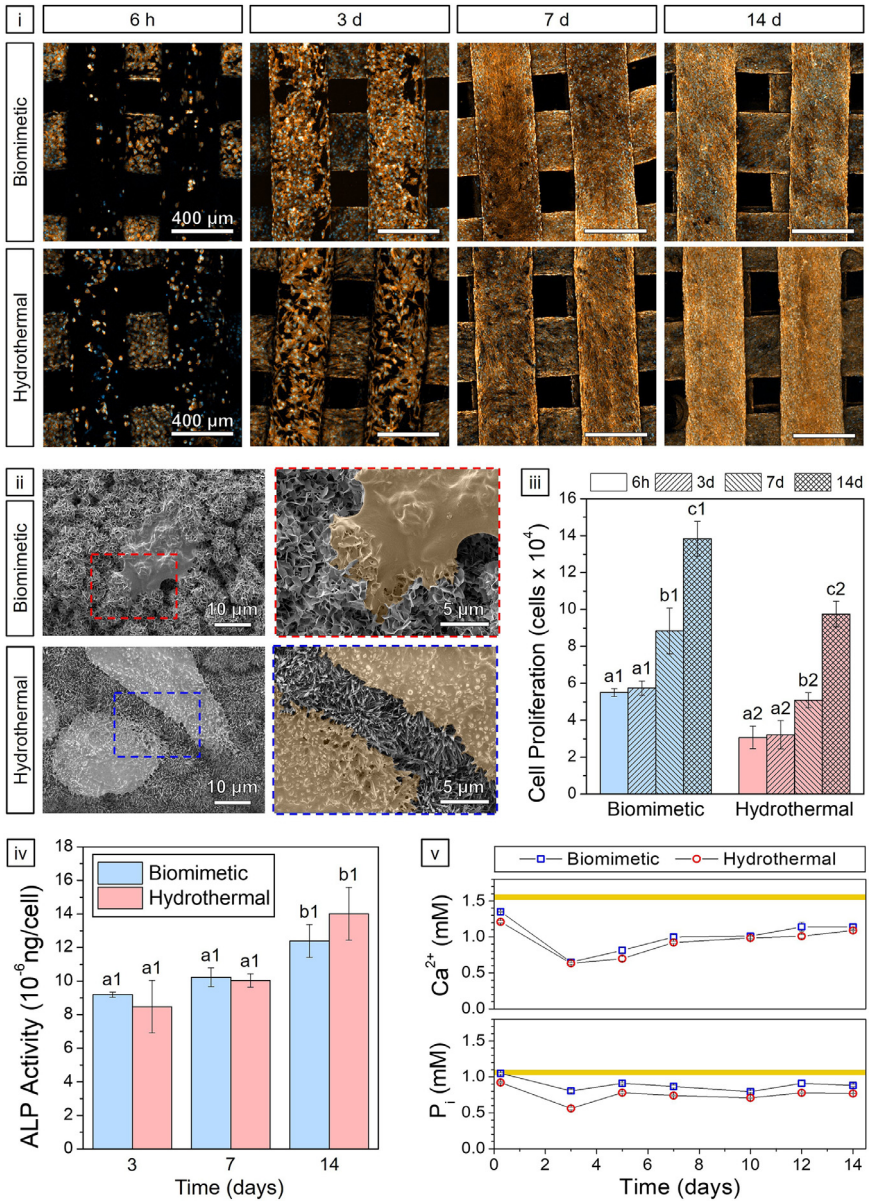

Fig. 7. *In vitro* study comparing the adhesion, proliferation and mineralisation of MG-63 cells on scaffolds consolidated with either the biomimetic or the hydrothermal treatment. (i) Fluorescent confocal microscopy images showing the cell adhesion and proliferation, with the nuclei appearing in light blue and the cytoskeleton in orange. (ii) SEM images evidencing the cell adhesion to the different scaffold microstructures after 6 h of culture. Cells are coloured in orange in the magnified slices for better identification. (iii) Cell proliferation quantified by a resazurin-based method. (iv) Alkaline phosphatase (ALP) activity. (v) Calcium and phosphate concentrations in the cell culture media. Yellow lines indicate the original ionic concentration in the culture medium. In iii and iv different letters and numbers indicate statistically significant differences between timepoints and conditions, respectively. (For interpretation of the references to color in this figure legend, the reader is referred to the web version of this article.)

3.3.1. Histomorphometric assessment

The percentage of newly formed bone was quantified in three dimensions. Scaffolds hardened under hydrothermal conditions presented a significantly higher amount of newly formed bone with a 37.3±4.7% compared to the 28.8±5.3% obtained with the biomimetic treatment (Fig. 8i). A more detailed analysis of the bone distribution inside the scaffolds revealed that the percentage of bone was higher along the entire cross-section in the hydrothermal scaffolds as compared to the biomimetic ones, and that the difference was more pronounced at the external region of the scaffold, in contact with the surrounding bone (Fig. 8ii). This is in agreement with Fig. 8iii, where the colour maps representing the cumulative value of the average of the percentage of bone on the axial projection (*i.e.*, printing plane) for all the specimens are displayed.

3.3.2. Histological evaluation

Both scaffold types presented newly formed bone growing in direct contact with the biomaterial (Figs. 9 and 10) and a widespread blood vessels network dispersed inside the interconnected macroporosity (Fig. 10i–iii, vii–ix). The new bone was mainly found surrounding the biomaterial and accumulated in the strand intersections, and consisted of a mixture of woven bone and some lamellar structures. The regions of lamellar bone were more abundant in the hydrothermal specimens, with numerous Haversian channels surrounded by successive osteonal lamellae, as well as Howship's lacunae in the osseous surfaces of the larger vascular channels, suggestive of an active remodelling process. No signs of degradation of the biomaterial were observed in any of the conditions.

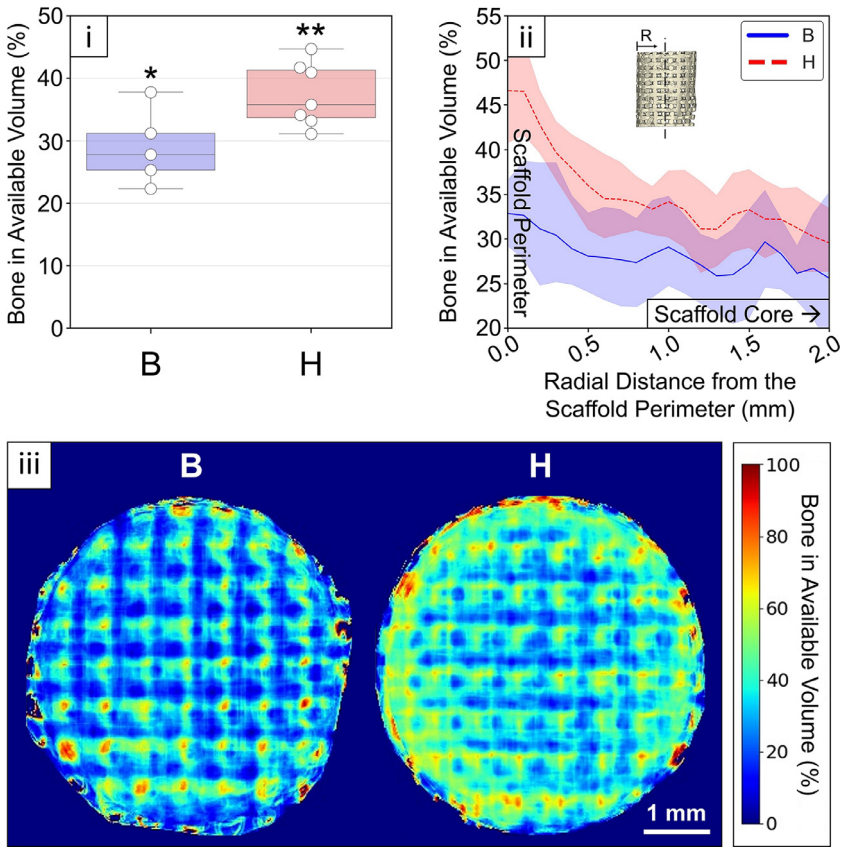

Fig. 8. μ-CT histomorphometric analysis: (i) Box plot and overlaid scatter plot of individual events representing the percentage of bone volume in available volume. Statistically significant differences indicated with a different number of asterisks (p-value = 0.024). (ii) Radial intrusion of bone into the scaffold. The X-axis represents the distance from the external perimeter of the scaffold. The average bone fraction is represented with a darker-coloured line and the 95% confidence interval for that estimate is represented with a softer-coloured region. (iii) Cumulative mapping showing the percentage of newly formed bone in available volume along the printing-plane projection (average of all the specimens).

4. Discussion

Using a hydrothermal hardening process for setting α-TCP-based synthetic bone grafts instead of the traditional biomimetic treatment is a strategy of major industrial interest as the processing time can be significantly reduced [33]. Moreover, contrary to what happens with high-temperature ceramic treatments, it allows obtaining solid structures with high specific surface areas and nanostructured surfaces, similarly to biomimetic treatments. The aim of this study was to shed light on the effects that the two treatments have at a chemical and structural level and especially in terms of the *in vivo* response.

4.1. Physicochemical properties

The hydrothermal treatment of the α-TCP - poloxamer green scaffolds resulted in two types of changes compared to the biomimetic route: slight alterations in the composition (Fig. 3) and a change in the shape of the precipitated crystals (Fig. 4). The differences in composition were attributed to an allotropic α-TCP to β-TCP transformation, associated with the temperature and pressure of the process, which coexist with the main reaction, the hydrolysis of α-TCP to CDHA [31]. Moreover, the higher reaction energy of this process favoured the nucleation of apatite with a higher crystallinity [52]. In addition, a small percentage of amorphous phase was detected ($\approx$ 10% for the hydrothermal and $\approx$ 7% for the biomimetic). The presence of intermediate amorphous phases has been previously detected in the precipitation of many apatitic products, including the hydrolysis of α-TCP, as they facilitate the nucleation of apatite crystals [53]. Moreover, accurate NMR and spectroscopic analyses on precipitated nanoapatite crystals have persistently observed an amorphous-like layer (hydrated-layer) covering the surface of existing nanocrystals. [28]. These two sources of amorphous content could explain the presence of amorphous phase detected in the samples.

Concerning the results from Raman spectroscopy, both scaffolds had very similar features in their phosphates, hydrogen phosphate and hydroxyl bands, despite the different hydrolysis settings: hydrothermal versus biomimetic. In both cases CDHA was characterised by a small hydroxyl band which, similar to biological bone apatites, indicates a very small amount of hydroxyl groups compared to highly pure stoichiometric hydroxyapatites [54]. This lack of OH^- ions is a common feature of non-stoichiometric calcium-deficient and hydroxyl- deficient apatites [55]. In addition, the HPO_4^{2-}, which is common in biological bone apatite (but not in stoichiometric hydroxyapatite) is also typically observed in the hydrolysis of α-TCP [56].

On the other hand, remarkable differences in crystal shape and size were observed. Whilst the biomimetic treatment led to plate-like structures, the hydrothermal setting resulted in needle-like crystals elongated along the *c*-axis and larger in size. Crystallite anisotropy for both, plates and needles, was confirmed by XRD, from the anomalously sharp peak corresponding to the (002) reflection (2θ = 25.9°), which indicates preferential crystal growth along the [001] direction, *i.e.*, along the *c*-axis. Similar results were previously reported [32,57–59]. Moreover, the crystallite size of the needle-shaped microstructure was approximately twice that of the plate-shaped one. The reason why the shape of the crystals is al-

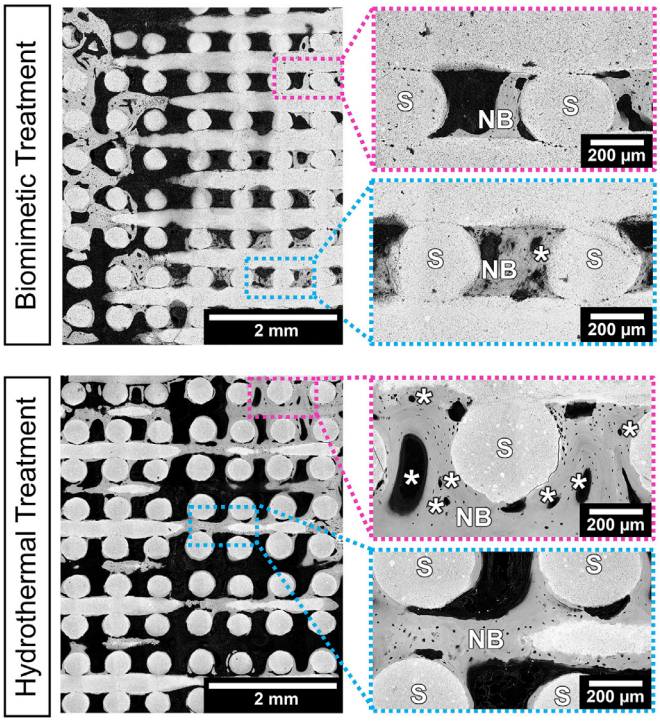

Fig. 9. Scanning electron micrographs of the scaffolds set through biomimetic and hydrothermal treatments after 8 weeks of implantation. The scaffold (S) appears in light grey in direct contact with the newly formed bone (NB), in darker grey. Haversian canals (asterisks) surrounded by concentrically arranged lamellae are visible in the regions where the bone is at a more advanced stage of remodelling.

tered is still unclear as too many variables such as temperature, pressure, pH, time, supersaturation, etc. can play a role. Moreover, the existence of negatively charged phosphate-rich *a*-surfaces and positively charged calcium-rich *c*-surfaces in hydroxyapatite leads to surface energy anisotropy, which also affects crystal growth. Ultimately, the morphology of the crystal depends on the competing growth of the *a*-surface *versus* the *c*-surface [32]. Analogously to the present observations, a similar difference in crystal morphology was observed when comparing calcium phosphates obtained by biomimetic setting treatments of α-TCP powders with fine and coarse particle sizes (*i.e.,* d_{50} = 2.22 and 10.88 µm, respectively). In that case, a smaller particle size led to a higher reactivity conducing to the nucleation of needle-shaped crystals, whereas larger particles were less reactive and resulted in the nucleation of plate-like crystals, although larger than those obtained in the present study [60].

The different crystal morphology had also implications in the pore size distribution recorded by MIP. Thus, the acicular crystals of the hydrothermal scaffolds gave rise to a more open and interconnected network, with larger pore entrance size (around 60–80 nm), and larger intrastrand porosity (57%) in contrast to the plate-shaped crystals of the biomimetic scaffolds, with very small pore entrance size (around 10-20 nm) and lower porosity (48%) (Fig. 5i), in agreement with previous results [61]. Although the differences in the amount of nanoporosity and nanopore size may appear small, they had a big impact on the interaction with physiological fluids, as revealed when analysing the BSA adsorption by the different substrates (Fig. 6). Whereas in the biomimetic scaffolds the protein was unable to enter the porous network in spite of its high porosity, the hydrothermal scaffolds were highly permeable to the diffusion of the protein, due to the higher porosity but, above all, the larger pore entrance size [62]. This resulted in a much higher amount of adsorbed protein in the H scaffolds despite their smaller specific surface area, a factor that may play a role in the distinct *in vivo* behaviour observed for the two materials notwithstanding the similarity in chemical composition.

Although poloxamer 407 is an FDA-approved compound categorised as an inactive ingredient with a multitude of pharmacological applications [63], the amount of poloxamer remaining in the final scaffolds was quantified in order to analyse if it could have any contribution to the observed biological results. The percentage of remaining binder was very small (less than 1 wt.%) compared to the 9.31 wt.% present in the initial ink. This indicates that the polymer was washed out during the setting step, while the samples were immersed in water, as it is water-soluble. Therefore, the differences observed in terms of biological performance cannot be associated with the presence of poloxamer in the scaffolds, as the amount differs in only 0.12 wt.% between experimental conditions.

4.2. Scaffold morphology and mechanical properties

Shrinkage is one of the most critical aspects that have to be closely monitored for the design of personalised bone grafts by 3D printing. After printing, the green bodies obtained by the extrusion of ceramic powder inks are normally subjected to drying and sintering treatments. Both, the removal of the binder and the formation of interparticle necks during the sintering process result in the shrinkage of the structure, and its magnitude depends on a multitude of factors, like the material, the ink solid fraction or the temperature and time of the thermal treatments among others [64], and typically ranges from 10 to 40% for DIW processes [15,65]. However, in the present work, the ink was composed of a reactive α-TCP powder, able to harden at a low temperature by a chemical consolidation process which allows circumventing the sintering step. As a result, much smaller shrinkages, below 3%, were recorded (Fig. 5ii).

The self-setting reaction is driven by the progressive dissolution of α-TCP and consequent precipitation of CDHA [21]. Fernandez *et al.* determined that the dimensional changes associated with the hydrolysis reaction of α-TCP to CDHA in calcium phosphate cements were as small as 0.10% [66]. Previous studies regarding its application to DIW considered shrinkage of these self-setting inks to be negligible [18,67]. Nonetheless, other works reported the existence of dimensional changes in the strands during the setting treatment, leading to longitudinal cracking [29,30]. To the best of our knowledge, the shrinkage associated with DIW calcium phosphate cement scaffolds had not been quantified so far.

In the present study, we were able to quantify by µ-CT a small but statistically significant linear shrinkage, more pronounced for the biomimetic scaffolds than for the hydrothermal ones, which was anisotropic, considerably larger in the X and Y printing directions than in the Z (vertical) direction (Fig. 5ii and iii). This small contraction may be the result of a combination of multiple events occurring at different stages of the scaffold fabrication process [68]: i) gravitational shrinkage, which may occur during the printing process when the ink still has not solidified. It is caused by the strand's own weight and it affects only the vertical direction (Z) [69–71]; ii) evaporation shrinkage, which may take place just after extrusion due to the evaporation of the binder's solvent. It gives rise to longitudinal shrinkage, which affects mainly the printing plane directions (*i.e.*, X and Y) [68]; iii) shrinkage linked to the removal of the binder by release in solution during the setting treatment. Some authors have reported swelling instead of contraction associated with the interaction of the binder with water [29,30]; iv) finally, dimensional changes associated with the consolidation process, in the present study the crystal entanglement during the cement-like reaction. These are much smaller than those observed in sintering processes due to the interparticle necking, and in both cases are isotropic [66,70,72].

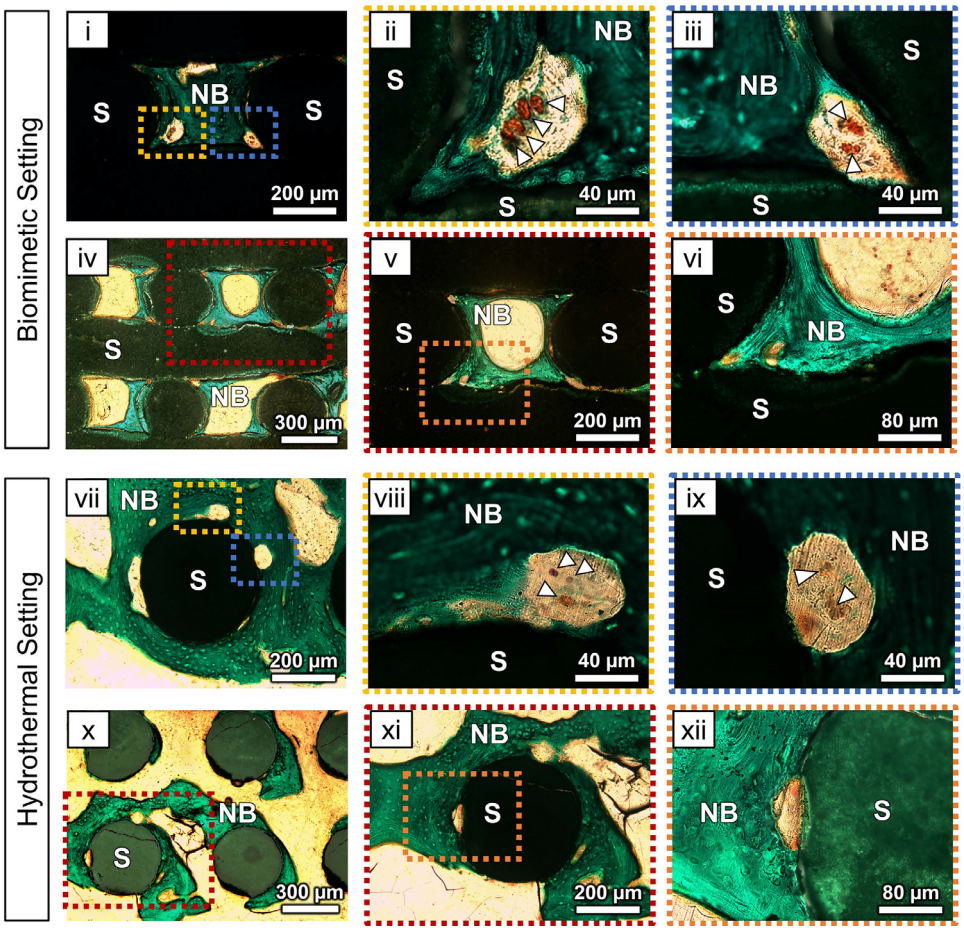

Fig. 10. Micrographs of undecalcified Masson-Goldner trichrome stained histological sections of biomimetically hardened (Top) and hydrothermally hardened (Bottom) 3D scaffolds. Both conditions showed a proper interaction of the scaffold (S) with the newly formed bone (NB), stained in green. Osteocytes inside lacunae are recognisable along all the calcified bone matrix and a network of blood vessels (white arrowheads) is identified in both materials (ii, iii, viii, ix). (For interpretation of the references to color in this figure legend, the reader is referred to the web version of this article.)

The small shrinkage detected in the present work was observed preferentially in the XY direction, and was negligible in the Z direction. This can be attributed on one hand to the robust gel-embedded powder suspension used, with pseudoplastic properties [73], and on another hand to the fixed layer height and the large layer overlap employed (25.7% of the strand diameter), which allowed each layer to compensate for potential vertical shrinkage in the previous layers. Similar trends were reported by other studies with calcium phosphate - poloxamer 407 inks, reporting more accentuated shrinkages in the printing plane directions than in the vertical direction [15,68]. The shrinkage observed could be associated with the evaporation of water during the printing process, or the release of the binder during the setting of the scaffolds. However, although the release of the binder when immersed in water during setting is almost total [33], this does not result in a high shrinkage, contrary to what happens during debinding for most ceramic inks. This could be explained by the fact that simultaneously with the binder dissolution, the reaction of the ceramic powder takes place, which results in the precipitation of an entangled network of newly precipitated crystals.

The difference between the two consolidation treatments was not statistically significant, although a more pronounced shrinkage was observed in the B condition. Although one possible reason could be a different degree of binder's washout during the two setting treatments, this was discarded due to the very similar amount of retained poloxamer, as revealed by the organic carbon content measurement. In the same vein, a previous study in reactive calcium phosphate robocasted structures observed different shrinkage behaviours attributed to different cement setting treatments [29]. Moreover, the higher shrinkage of the B condition is consistent with the smaller intrastrand porosity of the structure observed by MIP (Fig. 5i, Table 1). In summary, the precise determination of the shrinkage has confirmed the high dimensional stability associated with this type of inks and the advantage over the sintering-based approach. The values of shrinkage observed are compatible with the levels of shape accuracy required for patient-specific applications, as the resolution of the technique itself involves larger variability.

Regarding the mechanical properties, higher compressive and flexural strength were recorded for the hydrothermally treated scaffolds (Table 2). Since both scaffolds had similar total porosity, this trend seems to be associated with the levels of interstrand macroporosity, which was lower for the hydrothermal scaffolds than for the biomimetic ones, and affected the mechanical behaviour more markedly than the internal porosity of the strands, that was higher for the hydrothermal than for the biomimetic samples (Table 1). An additional parameter to be considered, besides porosity, is that the mechanical interlocking of the needle-shaped crystals can be more efficient than that provided by plate-like microstructures. This is in agreement with a previous study analysing the effect of the microstructure on the mechanical properties of calcium phosphate cements [60].

4.3. In vitro *performance*

A successful cell attachment and proliferation was achieved in both sample conditions, indicating the suitability of the two scaffold types for biological applications regardless of their different microstructures and composition. However, the higher initial cell adhesion in the biomimetically treated samples indicated that the plate-like crystals nanotopography was more favourable for the cell adhesion process. These results differ from previous studies comparing needle- and plate-like CDHA nanocrystals in flat specimens, where no cell adhesion differences were observed [35,74]. Nevertheless, in those studies the needle-shaped crystals were remarkably smaller than the plate-shaped counterparts, which is not the case in the present study. Regarding the ALP results, the increasing trend in both conditions evidences the ability of this type of materials to promote cell differentiation, which has been widely studied in the literature [34,75]. In spite of the preconditioning treatment applied, aimed at mitigating the detrimental effect that the ionic fluctuations may have on cells, the ionic interactions with the culture medium were not completely stopped. Similar observations have been reported in previous studies with CDHA, with a remarkable decrease of Ca^{2+} levels in the medium and smaller changes in the P_i concentration [46,76]. These are directly related to its non-stoichiometric nature, its low crystallinity and the high SSA. In contrast, in an *in vivo* scenario ionic exchange plays a key role in the bone regeneration process. In any case, it is important to highlight that, in spite of the different textural properties, the ionic exchange followed the same trend in the two materials studied. Therefore, it should not be considered as a possible cause of the differences observed *in vitro*, let alone *in vivo* where there is also a buffering effect and body fluids circulation [35].

4.4. In vivo *performance*

The histological evaluation showed bone growth in direct contact with both biomaterials. No evidence of fibrous encapsulation nor foreign body reaction were observed in any of the samples (Figs. 8 and 9). This confirms the biocompatibility of the low-temperature set (*i.e.,* hydrolysed) CDHA biomaterials, which has been already reported in several studies [25,27,77,78]. The newly formed bone was homogeneously distributed along the axial direction and followed a gradient in the radial direction, evidencing the osteoconductive properties of the material. Moreover, the interconnected porosity of the 3D-printed scaffolds allowed for the formation of widespread blood vessels along the structure.

Sanding the lateral faces of the scaffolds allowed to remove the edges with irregular and folded filaments and to obtain a structure composed of straight strands, reproducing the predominant arrangement of larger grafts used in a clinical scenario.

Performing a µ-CT-based volumetric quantification was crucial for a complete histomorphometric assessment of such a patterned structure. Unlike in isotropic architectures such as foams, where a two-dimensional analysis may be representative, in this case, the porosity of the cross-section is very dependent on the orientation. The percentages of bone found in the grafted structures (Fig. 8i) were similar to the ones found in the original trabecular defect region, assessed in the surrounding tissue. Additionally, this approach allowed to obtain further information to the classical bone surface over total surface (BS/TS) or bone volume over total volume (BV/TV) ratios. In this regard, bone intrusion could be assessed quantitatively (Fig. 8ii). No differences in the trend of the bone intrusion curves were identified between sample conditions, indicating that both materials presented similar osteoconduction properties. However, the vertical offset observed in the hydrothermal curve indicated a more advanced regeneration stage which is in agreement with the bone volume quantifications. Furthermore, the average bone percentage mappings corroborated both observations (Fig. 8iii). In both plots, a texture could also be identified which is associated with the pattern of the strands constituting the scaffold's structure.

In spite of the high similarity between the two materials compared, significantly higher percentages of newly formed bone were obtained in the hydrothermal condition (Fig. 8i). The distinctive features were the presence of 10% of β-TCP in the H samples, and the difference in microstructure, *i.e.* the needle-shaped vs plate-shaped morphology of the precipitated crystals in the H and B samples, respectively, as well as a lower SSA for the former. Regarding the presence of β-TCP, one could hypothesise that it could increase the release of calcium in the surrounding tissues due to its higher solubility. However, previous studies showed that despite having a higher solubility, the release of Ca from β-TCP was smaller than that from biomimetic CDHA due to the poor crystallinity and higher SSA of the latter [79]. Moreover, when increasing amounts of β-TCP were introduced in CDHA cements it was shown that calcium release was unaffected since β-TCP remained hidden within the CDHA matrix, which is also the case in the present material [80]. For these reasons, it seems that the cause of the different behaviours should rather be associated with the microstructural changes. Previous *in vivo* studies found a direct correlation between the microstructure of calcium phosphates and the bone regeneration process, being the needle-shaped microstructures the ones presenting the most promising results [34,36,81–83]. Specifically, in agreement with the results obtained in the present work, an earlier study comparing biomimetic CDHA with needle-like crystals vs plate-like crystals concluded that the needle-shaped microstructure resulted in accelerated osteoinductive and osteogenic properties [35]. This evidence of the benefits of the needle-like morphology has led to the development of hydrothermal methods for the production of microtextured coatings on stable calcium phosphate ceramics such as biphasic calcium phosphates [81].

One aspect that could also contribute to the distinct *in vivo* behaviour is the fact that the two scaffold types exhibited large differences in permeability to physiological fluids and soluble proteins, as seen in the BSA adsorption study. This is known to be a relevant factor regarding osteogenesis, where soluble proteins play a crucial role [84,85]. Specifically, many non-collagenous bone proteins (*e.g.*, bone morphogenetic proteins, osteocalcin, bone sialoprotein and fibronectin) play a major role in the bone formation process, triggering different steps of the cascade, and modulating the mineralisation process through their particular conformation and negative charge, which allows creating coordinating bonds with calcium cations [86]. In this sense, the extremely low permeability of the biomimetic scaffolds may be considered a detrimental aspect for their *in vivo* performance.

Finally, the morphological features of the osseous tissue found in the hydrothermal samples suggested a higher level of maturity. A larger number of lamellae was visible surrounding the Haversian channels of the larger and numerous osteons (Fig. 8). The cement lines visible in the lamellar bone around the scaffolds (Fig. 9) further indicated a more advanced stage in the bone remodelling process. The bone present in the biomimetic samples was mostly woven bone, with some osteons surrounded by a limited number of lamellae (Fig. 8).

5. Conclusion

The aim of this work was to compare two different hardening processes in 3D-printed CDHA scaffolds: one biomimetic and another hydrothermal. For the first time, we quantified the shrinkage associated with the α-TCP setting reaction to CDHA on 3D-printed scaffolds, concluding that it represents a minimal distortion to

the global scaffoldś structure. Both the biomimetic and hydrothermal treatments resulted in biocompatible scaffolds with osteoconductive properties. However, the differences in the microstructure, nanoporosity and nanopore size turned out to be key in both the interaction with proteins in solution and the osteogenic capacity of the materials. The specific features obtained by the hydrothermal process were found to be more favourable, resulting in significantly more bone. The implications for the clinical translation are clear, due to the reduced processing times required in the hydrothermal routes compared to the widely studied biomimetic methods.

Declaration of Competing Interest

YR and ET are employees of Mimetis Biomaterials S.L. amd MPG has an equity interest in Mimetis Biomaterials, S.L., a spin-off company of UPC that may potentially benefit from the research results displayed in the present work.

CRediT authorship contribution statement

Yago Raymond: Conceptualization, Investigation, Formal analysis, Data curation, Writing – original draft. **Mar Bonany:** Investigation, Formal analysis. **Cyril Lehmann:** Investigation. **Emilie Thorel:** Investigation. **Raúl Benítez:** Methodology, Formal analysis. **Jordi Franch:** Conceptualization, Investigation, Funding acquisition. **Montserrat Espanol:** Formal analysis. **Xavi Solé-Martí:** Investigation. **Maria-Cristina Manzanares:** Formal analysis. **Cristina Canal:** Funding acquisition, Writing – review & editing. **Maria-Pau Ginebra:** Conceptualization, Writing – review & editing, Supervision, Funding acquisition.

Acknowledgements

The authors acknowledge the Spanish Government for financial support through the PID2019-103892RB-I00/AEI/10.13039/501100011033 project. They also thank the Generalitat the Catalunya for funding through projects 2017SGR-1165 and BASE3D 001-P-001646 co-funded by European Regional Development Funds. YR acknowledges the Spanish Government for the PhD grant DI-15-08184. ME acknowledges the Serra Hunter Fellowship from the Generalitat de Catalunya. MPG and CC acknowledge the Generalitat de Catalunya for the ICREA Academia Award. The authors are thankful to the surgical team of the Veterinary Faculty at Universitat Autònoma de Barcelona for their collaboration with the animal's surgeries and housing. The authors are also grateful to Dr. Araceli Aznar and Dr. Trifon Trifonov from Barcelona Research Center in Multiscale Science and Engineering at Universitat Politècnica de Catalunya for their technical assistance with the μ-CT and SEM, respectively. The authors thank the support of Radu Trăscău with the image processing and Christian Guirola for proofreading the text.

Supplementary materials

Supplementary material associated with this article can be found, in the online version, at doi:10.1016/j.actbio.2021.09.001.

References

[1] C.L. Ventola, Medical applications for 3D printing: current and projected uses., P T. 39 (2014) 704–11. http://www.ncbi.nlm.nih.gov/pubmed/25336867.
[2] D.A. Hidalgo, Fibula free flap: a new method of mandible reconstruction, Plast. Reconstr. Surg. 84 (1989) 71–79 http://www.ncbi.nlm.nih.gov/pubmed/2734406.
[3] M.K. Sen, T. Miclau, Autologous iliac crest bone graft: Should it still be the gold standard for treating nonunions? Injury 38 (2007) S75–S80, doi:10.1016/j.injury.2007.02.012.
[4] P. Felice, C. Marchetti, G. Iezzi, A. Piattelli, H. Worthington, G. Pellegrino, M. Esposito, Vertical ridge augmentation of the atrophic posterior mandible with interpositional bloc grafts: bone from the iliac crest vs. bovine anorganic bone. Clinical and histological results up to one year after loading from a randomized-controlled clinical tria, Clin. Oral Implants Res. 20 (2009) 1386–1393, doi:10.1111/j.1600-0501.2009.01765.x.
[5] J. Parthasarathy, 3D modeling, custom implants and its future perspectives in craniofacial surgery, Ann. Maxillofac. Surg. 4 (2014) 9, doi:10.4103/2231-0746.133065.
[6] R.J. Mobbs, M. Coughlan, R. Thompson, C.E. Sutterlin, K. Phan, The utility of 3D printing for surgical planning and patient-specific implant design for complex spinal pathologies: case report, J. Neurosurg. Spine 26 (2017) 513–518, doi:10.3171/2016.9.SPINE16371.
[7] H. Saijo, K. Igawa, Y. Kanno, Y. Mori, K. Kondo, K. Shimizu, S. Suzuki, D. Chikazu, M. Iino, M. Anzai, N. Sasaki, U. Chung, T. Takato, Maxillofacial reconstruction using custom-made artificial bones fabricated by inkjet printing technology, J. Artif. Organs. 12 (2009) 200–205, doi:10.1007/s10047-009-0462-7.
[8] J. Cesarano, J.G. Dellinger, M.P. Saavedra, D.D. Gill, R.D. Jamison, B.A. Grosser, J.M. Sinn-Hanlon, M.S. Goldwasser, Customization of load-bearing hydroxyapatite lattice scaffolds, Int. J. Appl. Ceram. Technol. 2 (2005) 212–220, doi:10.1111/j.1744-7402.2005.02026.x.
[9] P. Tack, J. Victor, P. Gemmel, L. Annemans, 3D-printing techniques in a medical setting: a systematic literature review, Biomed. Eng. Online 15 (2016) 115, doi:10.1186/s12938-016-0236-4.
[10] N. Martelli, C. Serrano, H. van den Brink, J. Pineau, P. Prognon, I. Borget, S. El Batti, Advantages and disadvantages of 3-dimensional printing in surgery: a systematic review, Surgery 159 (2016) 1485–1500, doi:10.1016/j.surg.2015.12.017.
[11] J.C. Banwart, M.A. Asher, R.S. Hassanein, Iliac crest bone graft harvest donor site morbidity, Spine (Phila. Pa. 1976). 20 (1995) 1055–1060. doi:10.1097/00007632-199505000-00012.
[12] J.P. Anthony, J.D. Rawnsley, P. Benhaim, E.F. Ritter, S.H. Sadowsky, M.I. Singer, Donor leg morbidity and function after fibula free flap mandible reconstruction, Plast. Reconstr. Surg. 96 (1995) 146–152, doi:10.1097/00006534-199507000-00022.
[13] J.A. Lewis, G.M. Gratson, Direct writing in three dimensions, Mater. Today 7 (2004) 32–39, doi:10.1016/S1369-7021(04)00344-X.
[14] P. Miranda, E. Saiz, K. Gryn, A.P. Tomsia, Sintering and robocasting of β-tricalcium phosphate scaffolds for orthopaedic applications, Acta Biomater. 2 (2006) 457–466, doi:10.1016/j.actbio.2006.02.004.
[15] J. Franco, P. Hunger, M.E. Launey, A.P. Tomsia, E. Saiz, Direct write assembly of calcium phosphate scaffolds using a water-based hydrogel, Acta Biomater. 6 (2010) 218–228, doi:10.1016/j.actbio.2009.06.031.
[16] C.F. Marques, F.H. Perera, A. Marote, S. Ferreira, S.I. Vieira, S. Olhero, P. Miranda, J.M.F. Ferreira, Biphasic calcium phosphate scaffolds fabricated by direct write assembly: mechanical, anti-microbial and osteoblastic properties, J. Eur. Ceram. Soc. 37 (2017) 359–368, doi:10.1016/j.jeurceramsoc.2016.08.018.
[17] M. Vallet-Regí, J.M. González-Calbet, Calcium phosphates as substitution of bone tissues, Prog. Solid State Chem. 32 (2004) 1–31, doi:10.1016/j.progsolidstchem.2004.07.001.
[18] A. Lode, K. Meissner, Y. Luo, F. Sonntag, S. Glorius, B. Nies, C. Vater, F. Despang, T. Hanke, M. Gelinsky, Fabrication of porous scaffolds by three-dimensional plotting of a pasty calcium phosphate bone cement under mild conditions, J. Tissue Eng. Regen. Med. 8 (2014) 682–693, doi:10.1002/term.1563.
[19] Y. Maazouz, E.B. Montufar, J. Guillem-Marti, I. Fleps, C. Öhman, C. Persson, M.P. Ginebra, Robocasting of biomimetic hydroxyapatite scaffolds using self-setting inks, J. Mater. Chem. B 2 (2014) 5378–5386, doi:10.1039/C4TB00438H.
[20] J.M. Sadowska, J. Guillem-Marti, E.B. Montufar, M. Espanol, M.-P. Ginebra, Biomimetic versus sintered calcium phosphates: the *in vitro* behavior of osteoblasts and mesenchymal stem cells, Tissue Eng. Part A 23 (2017), doi:10.1089/ten.tea.2016.0406.
[21] M.P. Ginebra, E. Fernández, E.A.P. De Maeyer, R.M.H. Verbeeck, M.G. Boltong, J. Ginebra, F.C.M. Driessens, J.A. Planell, Setting reaction and hardening of an apatitic calcium phosphate cement, J. Dent. Res. 76 (1997) 905–912, doi:10.1177/00220345970760041201.
[22] M.-P. Ginebra, M. Espanol, Y. Maazouz, V. Bergez, D. Pastorino, Bioceramics and bone healing, EFORT Open Rev. 3 (2018) 173–183, doi:10.1302/2058-5241.3.170056.
[23] J.-P. Carrel, A. Wiskott, S. Scherrer, S. Durual, Large bone vertical augmentation using a three-dimensional printed TCP/HA bone graft: a pilot study in dog mandible, Clin. Implant Dent. Relat. Res. 18 (2016) 1183–1192, doi:10.1111/cid.12394.
[24] J.-P. Carrel, A. Wiskott, M. Moussa, P. Rieder, S. Scherrer, S. Durual, A 3D printed TCP/HA structure as a new osteoconductive scaffold for vertical bone augmentation, Clin. Oral Implants Res. 27 (2016) 55–62, doi:10.1111/clr.12503.
[25] P. Diloksumpan, R.V. Bolaños, S. Cokelaere, B. Pouran, J. de Grauw, M. van Rijen, R. van Weeren, R. Levato, J. Malda, Orthotopic bone regeneration within 3D printed bioceramic scaffolds with region-dependent porosity gradients in an equine model, Adv. Healthc. Mater. 1901807 (2020) 1–11, doi:10.1002/adhm.201901807.
[26] L. Vidal, C. Kampleitner, S. Krissian, M.Á. Brennan, O. Hoffmann, Y. Raymond, Y. Maazouz, M.-P. Ginebra, P. Rosset, P. Layrolle, Regeneration of segmental defects in metatarsus of sheep with vascularized and customized 3D-printed calcium phosphate scaffolds, Sci. Rep. 10 (2020) 7068, doi:10.1038/s41598-020-63742-w.

[27] A. Barba, Y. Maazouz, A. Diez-Escudero, K. Rappe, M. Espanol, E.B. Montufar, C. Öhman-Mägi, C. Persson, P. Fontecha, M.-C. Manzanares, J. Franch, M.-P. Ginebra, Osteogenesis by foamed and 3D-printed nanostructured calcium phosphate scaffolds: effect of pore architecture, Acta Biomater. 79 (2018) 135–147, doi:10.1016/j.actbio.2018.09.003.
[28] T. Ahlfeld, A. Lode, R.F. Richter, W. Pradel, A. Franke, M. Rauner, B. Stadlinger, G. Lauer, M. Gelinsky, P. Korn, Toward biofabrication of resorbable implants consisting of a calcium phosphate cement and fibrin—a characterization in vitro and in vivo, Int. J. Mol. Sci. 22 (2021) 1218, doi:10.3390/ijms22031218.
[29] A.R. Akkineni, Y. Luo, M. Schumacher, B. Nies, A. Lode, M. Gelinsky, A. Rahul, Y. Luo, M. Schumacher, B. Nies, A. Lode, M. Gelinsky, 3D plotting of growth factor loaded calcium phosphate cement scaffolds, Acta Biomater. (2015), doi:10.1016/j.actbio.2015.08.036.
[30] T. Ahlfeld, A.R. Akkineni, Y. Förster, T. Köhler, S. Knaack, M. Gelinsky, A. Lode, Design and Fabrication of complex scaffolds for bone defect healing: combined 3D plotting of a calcium phosphate cement and a growth factor-loaded hydrogel, Ann. Biomed. Eng. 45 (2017) 224–236, doi:10.1007/s10439-016-1685-4.
[31] L. Galea, D. Alexeev, M. Bohner, N. Doebelin, A.R.A.R. Studart, C.G. Aneziris, T. Graule, Textured and hierarchically structured calcium phosphate ceramic blocks through hydrothermal treatment, Biomaterials 67 (2015) 93–103, doi:10.1016/j.biomaterials.2015.07.026.
[32] S. Murakami, K. Kato, Y. Enari, M. Kamitakahara, N. Watanabe, K. Ioku, Hydrothermal synthesis of porous hydroxyapatite ceramics composed of rod-shaped particles and evaluation of their fracture behavior, Ceram. Int. 38 (2012) 1649–1654, doi:10.1016/j.ceramint.2011.09.056.
[33] S. Raymond, Y. Maazouz, E.B. Montufar, R.A. Perez, B. González, J. Konka, J. Kaiser, M. Ginebra, Accelerated hardening of nanotextured 3D-plotted self-setting calcium phosphate inks, Acta Biomater. 75 (2018) 451–462, doi:10.1016/j.actbio.2018.05.042.
[34] A. Barba, A. Diez-Escudero, Y. Maazouz, K. Rappe, M. Espanol, E.B. Montufar, M. Bonany, J.M. Sadowska, J. Guillem-Marti, C. Öhman-Mägi, C. Persson, M.-C. Manzanares, J. Franch, M.-P. Ginebra, Osteoinduction by foamed and 3D-Printed calcium phosphate scaffolds: effect of nanostructure and pore architecture, ACS Appl. Mater. Interfaces 9 (2017) 41722–41736, doi:10.1021/acsami.7b14175.
[35] A. Barba, A. Diez-Escudero, M. Espanol, M. Bonany, J.M. Sadowska, J. Guillem-Marti, C. Öhman-Mägi, C. Persson, M.C. Manzanares, J. Franch, M.P. Ginebra, Impact of biomimicry in the design of osteoinductive bone substitutes: nanoscale matters, ACS Appl. Mater. Interfaces 11 (2019) 8818–8830, doi:10.1021/acsami.8b20749.
[36] N. Davison, X. Luo, T. Schoenmaker, V. Everts, H. Yuan, F. Barrère-de Groot, de Bruijn, Submicron-scale surface architecture of tricalcium phosphate directs osteogenesis in vitro and in vivo, Eur. Cells Mater. 27 (2014) 281–297, doi:10.22203/eCM.v027a20.
[37] R. Duan, D. Barbieri, X. Luo, J. Weng, J.D. de Bruijn, H. Yuan, Submicron-surface structured tricalcium phosphate ceramic enhances the bone regeneration in canine spine environment, J. Orthop. Res. 34 (2016) 1865–1873, doi:10.1002/jor.23201.
[38] Y. Raymond, E. Thorel, M. Liversain, A. Riveiro, J. Pou, M.-P. Ginebra, 3D printing non-cylindrical strands: morphological and structural implications, Addit. Manuf. 46 (2021) 102129, doi:10.1016/j.addma.2021.102129.
[39] T. Westphal, T. Füllmann, H. Pöllmann, Rietveld quantification of amorphous portions with an internal standard—Mathematical consequences of the experimental approach, Powder Diffr. 24 (2009) 239–243, doi:10.1154/1.3187828.
[40] PANalytical B.V., X'Pert HighScore Plus Help System Version 3.0. Operations Manual, 2009.
[41] G. Caglioti, A. Paoletti, F.P. Ricci, Choice of collimators for a crystal spectrometer for neutron diffraction, Nucl. Instrum. 3 (1958) 223–228, doi:10.1016/0369-643X(58)90029-X.
[42] C.T. Rueden, J. Schindelin, M.C. Hiner, B.E. DeZonia, A.E. Walter, E.T. Arena, K.W. Eliceiri, ImageJ2: ImageJ for the next generation of scientific image data, BMC Bioinf. 18 (2017) 529, doi:10.1186/s12859-017-1934-z.
[43] A. Fedorov, R. Beichel, J. Kalpathy-Cramer, J. Finet, J.C. Fillion-Robin, S. Pujol, C. Bauer, D. Jennings, F. Fennessy, M. Sonka, J. Buatti, S. Aylward, J.V. Miller, S. Pieper, R. Kikinis, 3D slicer as an image computing platform for the quantitative imaging network, Magn. Reson. Imag. 30 (2012) 1323–1341, doi:10.1016/j.mri.2012.05.001.
[44] International Organization for Standardization, 14704:2016 Fine ceramics (advanced ceramics, advanced technical ceramics) — Test method for flexural strength of monolithic ceramics at room temperature, 2016.
[45] J. Gustavsson, M.P. Ginebra, E. Engel, J. Planell, Ion reactivity of calcium-deficient hydroxyapatite in standard cell culture media, Acta Biomater 7 (2011) 4242–4252, doi:10.1016/j.actbio.2011.07.016.
[46] J.M. Sadowska, J. Guillem-Marti, M. Espanol, C. Stähli, N. Döbelin, M.-P. Ginebra, In vitro response of mesenchymal stem cells to biomimetic hydroxyapatite substrates: a new strategy to assess the effect of ion exchange, Acta Biomater. 76 (2018) 319–332, doi:10.1016/j.actbio.2018.06.025.
[47] N.R. CouncilGuide for the Care and Use of Laboratory Animals, National Academies Press, Washington, D.C., 2011, doi:10.17226/12910.
[48] C. Bishop, Pattern Recognition and Machine Learning, Springer, 2005.
[49] R.C. Gonzalez, R.E. Woods, Digital Image Processing, 4th Editio, Pearson, 2018.
[50] S. Koutsopoulos, Synthesis and characterization of hydroxyapatite crystals: A review study on the analytical methods, J. Biomed. Mater. Res. 62 (2002) 600–612, doi:10.1002/jbm.10280.
[51] M. Markovic, B.O. Fowler, M.S. Tung, Preparation and comprehensive characterization of a calcium hydroxyapatite reference material, J. Res. Natl. Inst. Stand. Technol. 109 (2004) 553, doi:10.6028/jres.109.042.
[52] L.M. Rodríguez-Lorenzo, M. Vallet-Regí, Controlled crystallization of calcium phosphate apatites, Chem. Mater. 12 (2000) 2460–2465, doi:10.1021/cm001033g.
[53] X. Wei, O. Ugurlu, M. Akinc, Hydrolysis of α-tricalcium phosphate in simulated body fluid and dehydration behavior during the drying process, J. Am. Ceram. Soc. 90 (2007) 2315–2321, doi:10.1111/j.1551-2916.2007.01682.x.
[54] C. Rey, C. Combes, C. Drouet, M.J. Glimcher, Bone mineral: update on chemical composition and structure, Osteoporos. Int. 20 (2009) 1013–1021, doi:10.1007/s00198-009-0860-y.
[55] C. Drouet, Apatite formation: why it may not work as planned, and how to conclusively identify apatite compounds, Biomed Res. Int. 2013 (2013) 1–12, doi:10.1155/2013/490946.
[56] M. Espanol, J. Portillo, J.-M. Manero, M.-P. Ginebra, Investigation of the hydroxyapatite obtained as hydrolysis product of α-tricalcium phosphate by transmission electron microscopy, CrystEngComm 12 (2010) 3318, doi:10.1039/c001754j.
[57] M. Yoshimura, H. Suda, K. Okamoto, K. Ioku, Hydrothermal synthesis of biocompatible whiskers, J. Mater. Sci. 29 (1994) 3399–3402, doi:10.1007/BF00352039.
[58] K. Ioku, S. Nishimura, Y. Eguchi, S. Goto, Hydrothermal Preparation of Porous Hydroxyapatite Ceramics, Rev. HIGH Press. Sci. Technol. 7 (1998) 1398–1400, doi:10.4131/jshpreview.7.1398.
[59] K. Ioku, G. Kawachi, S. Sasaki, H. Fujimori, S. Goto, Hydrothermal preparation of tailored hydroxyapatite, J. Mater. Sci. 41 (2006) 1341–1344, doi:10.1007/s10853-006-7338-5.
[60] M.P. Ginebra, F.C.M. Driessens, J.A. Planell, Effect of the particle size on the micro and nanostructural features of a calcium phosphate cement: a kinetic analysis, Biomaterials 25 (2004) 3453–3462, doi:10.1016/j.biomaterials.2003.10.049.
[61] D. Pastorino, C. Canal, M.-P. Ginebra, Multiple characterization study on porosity and pore structure of calcium phosphate cements, Acta Biomater. 28 (2015) 205–214, doi:10.1016/j.actbio.2015.09.017.
[62] M. Espanol, R.A. Perez, E.B. Montufar, C. Marichal, A. Sacco, M.P. Ginebra, Intrinsic porosity of calcium phosphate cements and its significance for drug delivery and tissue engineering applications, Acta Biomater. 5 (2009) 2752–2762, doi:10.1016/j.actbio.2009.03.011.
[63] J.J. Escobar-Chávez, M. López-Cervantes, A. Naïk, Y.N. Kalia, D. Quintanar-Guerrero, A. Ganem-Quintanar, Applications of thermo-reversible pluronic F-127 gels in pharmaceutical formulations, J. Pharm. Pharm. Sci. 9 (2006) 339–358 http://www.ncbi.nlm.nih.gov/pubmed/17207417.
[64] F. Abdeljawad, D.S. Bolintineanu, A. Cook, H. Brown-Shaklee, C. DiAntonio, D. Kammler, A. Roach, Sintering processes in direct ink write additive manufacturing: a mesoscopic modeling approach, Acta Mater. 169 (2019) 60–75, doi:10.1016/j.actamat.2019.01.011.
[65] A. Nommeots-nomm, P.D. Lee, J.R. Jones, Journal of the european ceramic society direct ink writing of highly bioactive glasses, J. Eur. Ceram. Soc. 38 (2018) 837–844, doi:10.1016/j.jeurceramsoc.2017.08.006.
[66] E. Fernández, M.P. Ginebra, O. Bermúdez, M.G. Boltong, F.C.M. Driessens, J.A. Planell, Dimensional and thermal behaviour of calcium phosphate cements during setting compared to PMMA bone cements, J. Mater. Sci. Lett. 14 (1995) 4–5, doi:10.1007/BF02565267.
[67] N. Raja, A. Sung, H. Park, H. Yun, Low-temperature fabrication of calcium deficient hydroxyapatite bone scaffold by optimization of 3D printing conditions, Ceram. Int. 47 (2021) 7005–7016, doi:10.1016/j.ceramint.2020.11.051.
[68] E.B. Montufar, K. Slámečka, M. Casas-Luna, P. Skalka, E. Ramírez-Cedillo, M. Zbončák, J. Kaiser, L. Čelko, Factors governing the dimensional accuracy and fracture modes under compression of regular and shifted orthogonal scaffolds, J. Eur. Ceram. Soc. 40 (2020) 4923–4931, doi:10.1016/j.jeurceramsoc.2020.03.045.
[69] J. Cesarano, A review of robocasting technology, MRS Proc. 542 (1998) 133, doi:10.1557/PROC-542-133.
[70] S. Eqtesadi, A. Motealleh, F.H. Perera, P. Miranda, A. Pajares, R. Wendelbo, F. Guiberteau, A.L. Ortiz, Fabricating geometrically-complex B4C ceramic components by robocasting and pressureless spark plasma sintering (DOI MALAMENT REVISAR), Scr. Mater. 145 (2018) 14–18, doi:10.1016/j.scriptamat.2017.10.001.
[71] M. Houmard, Q. Fu, M. Genet, E. Saiz, A.P. Tomsia, On the structural, mechanical, and biodegradation properties of HA/β-TCP robocast scaffolds, J. Biomed. Mater. Res. Part B Appl. Biomater. 101 (2013) 1233–1242, doi:10.1002/jbm.b.32935.
[72] Á.D.E. Pablos, M. Belmonte, M.I. Osendi, P. Miranzo, Cerámica y Vidrio microstructural designs of spark-plasma sintered silicon carbide ceramic scaffolds, 53 (2014) 93–100. doi:10.3989/cyv.132014.
[73] E. Feilden, Additive manufacturing of ceramics and ceramic composites via robocasting, Imperial College London, 2017 https://spiral.imperial.ac.uk/handle/10044/1/55940.
[74] J.M. Sadowska, F. Wei, J. Guo, J. Guillem-Marti, M.-P. Ginebra, Y. Xiao, Effect of nano-structural properties of biomimetic hydroxyapatite on osteoimmunomodulation, Biomaterials 181 (2018) 318–332, doi:10.1016/j.biomaterials.2018.07.058.
[75] P. Habibovic, H. Yuan, C.M. van der Valk, G. Meijer, C. a van Blitterswijk, K. de Groot, 3D microenvironment as essential element for osteoinduction by bio-

materials, Biomaterials 26 (2005) 3565–3575, doi:10.1016/j.biomaterials.2004.09.056.

[76] G. Ciapetti, G. Di Pompo, S. Avnet, D. Martini, A. Diez-Escudero, E.B. Montufar, M.-P. Ginebra, N. Baldini, Osteoclast differentiation from human blood precursors on biomimetic calcium-phosphate substrates, Acta Biomater 50 (2017) 102–113, doi:10.1016/j.actbio.2016.12.013.

[77] H. GUO, J. SU, J. WEI, H. KONG, C. LIU, Biocompatibility and osteogenicity of degradable Ca-deficient hydroxyapatite scaffolds from calcium phosphate cement for bone tissue engineering, Acta Biomater 5 (2009) 268–278, doi:10.1016/j.actbio.2008.07.018.

[78] L. Ambrosio, V. Guarino, V. Sanginario, P. Torricelli, M. Fini, M.P. Ginebra, J. a Planell, R. Giardino, Injectable calcium-phosphate-based composites for skeletal bone treatments, Biomed. Mater. 7 (2012) 024113, doi:10.1088/1748-6041/7/2/024113.

[79] A. Diez-Escudero, M. Espanol, S. Beats, M.-P. Ginebra, In vitro degradation of calcium phosphates: Effect of multiscale porosity, textural properties and composition, Acta Biomater. 60 (2017) 81–92, doi:10.1016/j.actbio.2017.07.033.

[80] S. Gallinetti, C. Canal, M.-P. Ginebra, Development and characterization of biphasic hydroxyapatite/β- <scp>TCP</scp>Cements, J. Am. Ceram. Soc. 97 (2014) 1065–1073, doi:10.1111/jace.12861.

[81] R. Duan, L. van Dijk, D. Barbieri, F. de Groot, H. Yuan, J. de Bruijn, Accelerated bone formation by biphasic calcium phosphate with a novel sub-micron surface topography, Eur. Cells Mater. 37 (2019) 60–73, doi:10.22203/eCM.v037a05.

[82] N. Davison, J. Su, H. Yuan, J. van den Beucken, J. de Bruijn, F. Barrère-de Groot, Influence of surface microstructure and chemistry on osteoinduction and osteoclastogenesis by biphasic calcium phosphate discs, Eur. Cells Mater. 29 (2015) 314–329, doi:10.22203/eCM.v029a24.

[83] S.-I. Roohani-Esfahani, S. Nouri-Khorasani, Z. Lu, R. Appleyard, H. Zreiqat, The influence hydroxyapatite nanoparticle shape and size on the properties of biphasic calcium phosphate scaffolds coated with hydroxyapatite–PCL composites, Biomaterials 31 (2010) 5498–5509, doi:10.1016/j.biomaterials.2010.03.058.

[84] L.E. Rustom, T. Boudou, S. Lou, I. Pignot-Paintrand, B.W. Nemke, Y. Lu, M.D. Markel, C. Picart, A.J. Wagoner Johnson, Micropore-induced capillarity enhances bone distribution in vivo in biphasic calcium phosphate scaffolds, Acta Biomater. 44 (2016) 144–154, doi:10.1016/j.actbio.2016.08.025.

[85] S.K. Lan Levengood, S.J. Polak, M.B. Wheeler, A.J. Maki, S.G. Clark, R.D. Jamison, A.J. Wagoner Johnson, Multiscale osteointegration as a new paradigm for the design of calcium phosphate scaffolds for bone regeneration, Biomaterials 31 (2010) 3552–3563, doi:10.1016/j.biomaterials.2010.01.052.

[86] J. Benesch, J.F. Mano, R.L. Reis, Proteins and their peptide motifs in acellular apatite mineralization of scaffolds for tissue engineering, Tissue Eng. Part B Rev. 14 (2008) 433–445, doi:10.1089/ten.teb.2008.0121.